UNIVERSITÉ DE NEUCHÂTEL
INSTITUT DE MICROTECHNIQUE

Pattern recognition based on hybrid coherent optical and electronic information processing

THÈSE

PRÉSENTÉE A LA FACULTÉ DES SCIENCES
POUR OBTENIR LE GRADE DE DOCTEUR ÈS SCIENCES

PAR

Kurt Hess

Imprimerie Le Franc-Montagnard SA, 2726 Saignelégier
1986

IMPRIMATUR POUR LA THÈSE

Pattern Recognition Based on Hybrid Coherent Optical and Electronic Information Processing

de M*onsieur Kurt Hess*

UNIVERSITÉ DE NEUCHATEL

FACULTÉ DES SCIENCES

La Faculté des sciences de l'Université de Neuchâtel, sur le rapport des membres du jury,

Messieurs R. Dändliker, F. Pellandini, Y. Ruedin (Neuchâtel) et J.-Ch. Viénot (Besançon)

autorise l'impression de la présente thèse.

Neuchâtel, le *12 janvier 1986*

Le doyen:

François Sigrist

François Sigrist

Abstract

Two new concepts for on-line pattern recognition have been investigated. They use high speed coherent optical processing to generate the Fourier spectrum of the pattern to be recognized. Considerable data reduction is then obtained by carefully selecting the relevant information from the spectrum before optoelectronic detection. The final processing is performed electronically.

The first system extracts the information on shape and angular orientation from a circular scan of the shift invariant intensity distribution in the Fourier spectrum. The transverse position of the pattern is obtained by heterodyne detection of the linear phase term at the origin of the spectrum. This concept allows to identify reliably any pattern among a limited set of known patterns. Angular orientation and transverse position are determined with an accuracy of 0.5 deg and 1% of the extension of the field of view, respectively.

The second system identifies a pattern by comparing some low order irradiance moments with previousely stored reference values. These moments are deduced from the corresponding derivatives at the origin of the Fourier spectrum (moment theorem), which are obtained by sampling intensity and phase in the central part of the spectrum and fitting a polynomial of appropriate order to the sampled values. An experimental system was successfully tested, but reliable pattern recognition requires more accurate phase sampling (< 0.3 deg) or more samples (>12).

Table of contents

1. Introduction

Pattern recognition has been performed by the human visual sense for many thousands of years. This biological system had long been perfectly matched to its task in everydays life. Only recently man has learned to make machines and computers work for him. These tools have become versatile and even far more efficient than man for many tasks. The field of practical applications, however, could be considerably extended if they were provided with a visual sense. So there is a great need for a vision system which is better matched to technical apparatus than the biological one. Such systems are already successfully applied in robotics, evaluation of air photographs, recognition of biological cells and many other fields. They are, however, still far from matching the efficiency of the biological counterparts. The problem of expediently detecting and processing the large amount of image data has remained a challenge for scientists and engineers. The present work discribes a novel approach to do this task with high efficiency.

Among the various pattern recognition concepts that have been proposed in the past decades one finds two prominent examples: The first consists in scanning the 2-D image with a TV camera and processing the data in a digital computer. Such systems consist of well known standard elements and provide a considerable flexibility. Due to the serial detection and evaluation, however, they are inherently slow.

The second well known pattern recognition concept applies a coherent optical correlator invented by Vander Lugt [1]. It uses the 2-D Fourier transform properties of coherent optics and matched (object specific) holographic filters in the Fourier plane to yield correlations of edge enhanced images of the patterns. It offers high speed, on-line and in real time, at high spatial resolution, due to its inherently parallel processing of 2-D information. However the practical applications are limited mainly by the lack of flexibility of the filter function, which has to be realized in hardware.

A new class of hybrid systems tries to combine the high speed Fourier transform properties of coherent optics with the flexibility of digital programming. This can be obtained by placing the interface between optics and electronics in the Fourier plane and by carefully selecting the relevant

information before optoelectronic detection of the data to be processed electronically. The motivation to place the detectors in the Fourier plane rather than in the object plane is twofold: First, decoupling of the information on object shape and object shift, as a result of the shift theorem. Second, the local separation of the more and the less significant part of information in the Fourier spectrum. Both properties are favorable to a powerful data compression which is necessary for rapid electronic final processing. The use of this hybrid concept in on-line object tracking and recognition for robot vision will be discribed in the first part of this work. The corresponding investigations have given insight in the relations between object features and the properties of the Fourier spectrum. This knowledge was the base for the investigation of an object recognition system using two-dimensional irradiance moments of the image of the object. These moments are given by the derivatives of the Fourier spectrum at the origin. Invariant moments can be deduced for efficient pattern recognition, independent of orientation and size. A detailed description of the theoretical and experimental limitations of the determination of irradiance moments from intensity and phase measurements in the Fourier spectrum is given in the second part of this work.

2. Real-time object tracking and recognition

The basic task in robot vision is to identify an object and to determine its position from the 2-D image seen by the eye of the robot. As shown in Fig.1 the position of an object is given by the two coordinates x_s and y_s of the center of gravity and the angular orientation α_0. The object has to be identified within the ensemble of a limited number of known objects O_n. Real time means that the object must be recognized and located within less than 1 sec.

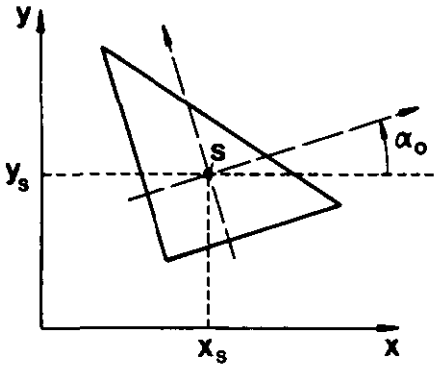

Fig.1. Angular orientation α_0 and lateral position x_s, y_s of the 2-D image of an object.

Solutions to the problem using coherent optical correlation have been described [1,2]. An incoherent image of the scene, containing the diffusely scattering object to be recognized, is formed by a first lens on the input face of an incoherent-to-coherent image transducer, in this case a liquid crystal light valve (LCLV). The coherent image is then optically Fourier transformed by a second lens. The object recognition is performed with the help of a holographically recorded matched filter in the Fourier plane which produces a correlation spot after transformation by a third lens. The position of that spot in the correlation plane is linearly related to the lateral position of the object. The position and the hight of the correlation peak are electrooptically detected by an arrangement of two orthogonal linear diode array detectors and gratings to produce 1-D images of the correlation space [3]. With this setup one object at a given angular orientation can be identified and its lateral position (x_s, y_s) determined.

Since the Fourier transform is not invariant to rotation, it is necessary to rotate the light field with respect to the filter. This can be done by an optical image rotator between the image transducer and the Fourier plane [3]. The angular orientation α_0 of the object is obtained from a search for the correlation peak by scanning the correlation space for every increment in angle of the image rotator. To identify several objects, individual holographic filters have to be employed for each object.

The main drawbacks of coherent optical correlation systems for object recognition and tracking may be summarized as follows:

-- Holographic recording of the matched filters (hardware programming);
-- Sequential search for the angular orientation by image rotation;
-- Individually matched filters for each object to be recognized (hardware addressing).

The hybrid system presented in Fig.2 eliminates these drawbacks by replacing the matched holographic filter (hardware) with electronic processing (software) of amplitude and phase detected in the Fourier transform [4].

Recognition and tracking is achieved as follows: In a first Fourier plane the power spectrum (intensity), which is known to be shift invariant, is observed (Fig.3a). A circular scan with a diode array detector yields a 1-D signature $P(\phi)$ (Fig.3b) of the object. The angular orientation α_0 and the identification of the object are then easily obtained by calculating the correlation with the stored signatures $P_n(\phi)$ of the reference objects. In a second Fourier plane the phase of the spectrum is measured by heterodyning with a reference wave shifted in frequency by about 40 kHz. With two pairs of photodetectors (Fig.9a) the linear phase shifts due to the translation x_s, y_s of the object can be determined in two orthogonal directions. The optical phase shifts are transformed by the heterodyne detection into the phase differences of sinusoidal signals (Fig.9b) which are easily measured electronically.

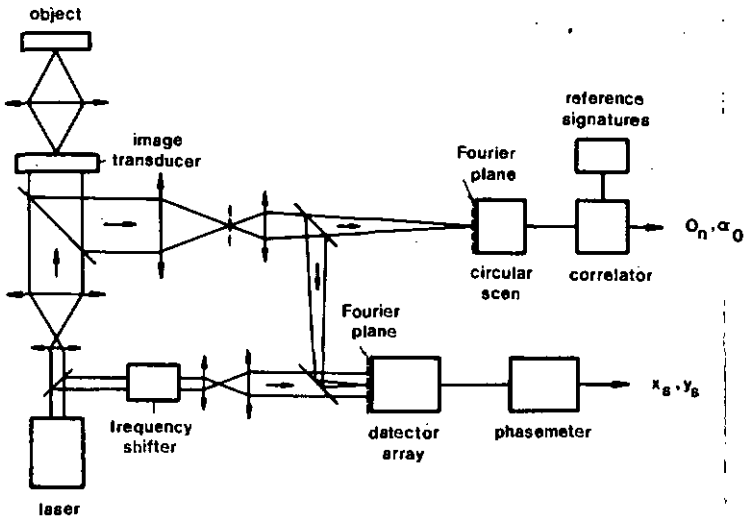

Fig.2. Hybrid optical electronic system for robot vision.

2.1 Power spectrum: Identification and angular orientation

2.1.1 Detection of significant intensity profiles

As shown in Fig.2, the shape and the angular orientation of an object are determined from the intensity distribution of the diffraction pattern. This is known to be shift invariant and centered at the origin of the Fourier plane. The complex amplitude of the light field in that plane is proportional to the 2-D Fourier transform,

$$\hat{O}(\vec{p}) = \int d^2x \; O(\vec{x}) \exp(-i2\pi\vec{p}\cdot\vec{x}) \; , \qquad (1)$$

of the coherent object function $O(\vec{x})$ in the input plane. The power spectrum $P(\rho,\phi)$, expressed in polar coordinates ρ and ϕ, is then given by

$$P(\rho,\phi) = |\hat{O}(\vec{p})|^2, \quad \rho = |\vec{p}| \; , \qquad (2)$$

independent of the lateral position $\vec{x}_s$ of the object $O(\vec{x} - \vec{x}_s)$. Rotating the object, however, rotates the power spectrum by the same angle. The angular orientation α_0 (Fig.1) and the identification of the object are obtained from a circular scan of the power spectrum (Fig.3a) at radius ρ_0. This yields a 1-D signature (Fig.3b),

$$P_0(\phi) = P(\rho_0, \phi) \ , \tag{3}$$

which can be compared with the previously stored signatures $P_n(\phi)$ of the reference objects O_n.

A small but significant part of the information in the Fourier spectrum is selected by the circular scan. Both high ond low spatial frequencies are ignored much like in matched spatial filtering. Slow phase or intensity variations across the object resulting from imperfect optical systems are thus much less troublesome. Note, however, that the determination of the angular orientation α_0 suffers from a 180 deg ambiguity for real-valued object functions $O(\vec{x})$ because of the central symmetry of the power spectrum. The asymmetric aspects of such objects can only be recognized from the phase of the Fourier transform, which will be discussed in Sec. 2.2.3.

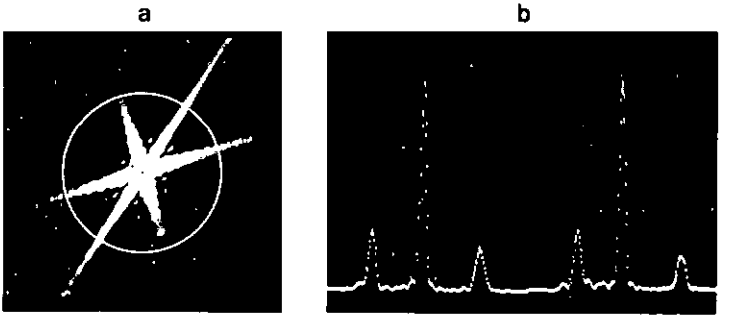

Fig.3. Power spectrum (intensity): (a) circular scan, (b) signature $P_0(\phi)$.

Fig.3 shows the power spectrum $P(\rho,\phi)$ and the signature $P_0(\phi)$ of a triangular object. The scan was made by a Reticon RO-720 circular photodiode array [5]. It has 720 diodes of 250 um radial length, 20 um width, and 30 um spacing (center to center) on a circle of 3.44 mm radius. The scan radius ρ_0 was chosen to be about six times the average radius ρ_c of the zero-order diffraction spot ($\rho_0 \approx 6\rho_c$), which is inversely proportional to the overall size of the object. Since the fine structures of the spectrum have about half the size of the zero-order spot, the detector ring covers about one-third of such an element and the peaks in the signature $P_0(\phi)$ (Fig.3b) are about 20 diodes wide. The example shown in Fig.3 corresponds to 0.2 mW light from a He-Ne laser passing through a triangular opening cut out of a metal plate. The circular photodiode array was scanned at a rate of 80 Hz.

2.1.2 Correlation and discrimination

Shape and angular orientation of an object are determined through correlation of its signature $P_0(\phi)$ with all the previously stored signatures $P_n(\phi)$ of the reference objects O_n. If one and only one peak of the correlation functions exceeds a preset threshold, the object is identified and its orientation is given by the angular position of this peak value. Note that two circular, and thus endless, profiles have to be correlated for this purpose. Proper normalization should be used to obtain unity auto-correlation peak values, independent of the intensity level. The following definition for the correlation function $C_n(\alpha)$ fulfills the above conditions:

$$C_n(\alpha) = \int d\phi \; P_0(\phi) \; P_n(\phi - \alpha) \; / \; p_0 \; p_n \quad , \tag{4}$$

$$\text{with} \quad p_0^2 = \int d\phi \; P_0^2(\phi) \quad \text{and} \quad p_n^2 = \int d\phi \; P_n^2(\phi) \; .$$

The discrete version of Eq.(4) used in the present work is

$$C_n(\alpha_k) = \sum_{i=1}^{N} P_0(\phi_i) \; P_n(\phi_j) \; / \; p_0 \; p_n \quad , \tag{5}$$

$$\text{with} \quad j = [(i-k+N-1) \bmod (N)] + 1 \quad ,$$

$$p_0^2 = \sum_{i=1}^{N} [(P_0(\phi_i)]^2 \quad \text{and} \quad p_n^2 = \sum_{i=1}^{N} [P_n(\phi_i)]^2 \; ,$$

N = number of resolved angular positions.

The properties of the so defined correlation functions can be estimated from the fact that the values $C_n(\alpha_k)$ are given by a scalar product of the two normalized N-dimensional vectors $\vec{P}_0/p_0$ and $\vec{P}_n/p_n$. This means that $C_n(\alpha_k) \leq 1$, where only the auto-correlation peak value $C_0(\alpha_0)$ is equal to unity. Fig.4 shows a digitized (8 bit) signature $P_0(\Phi)$ and the corresponding auto-correlation calculated with an angular resolution N of 72 points per half circle.

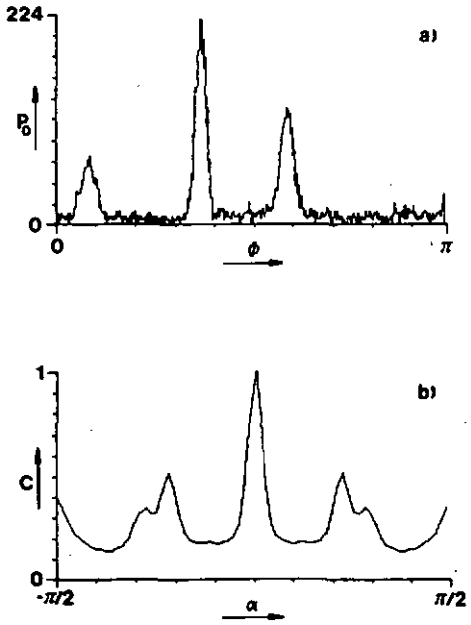

Fig.4. Digital correlation of signatures: (a) digitized signature $P_0(\Phi)$. (b) auto-correlation of $P_0(\Phi)$.

Different algorithms may be used to calculate position and hight of the correlation peaks. Since the number of multiplications to be performed for $C_n(\alpha)$ in Eq.(5) increases as N^2, where N is the number of resolved angular positions, it might be advisable to calculate first an approximate position of the peak at reduced angular resolution and then do high resolution correlation

only in the neighbourhood of the peak. This iterative approach reduces not only the time needed for the calculation but produces faster useful information for the robot system. Binary versions of the reference signatures may be applied to avoid any numerical multiplication in the calculation of the correlation (Sec.2.1.3).

2.1.3 Experimental results

For experimental tests of that concept, four binary objects $O(\vec{x})$ (structured openings in metal plates), representing different classes of shape, were chosen. They were placed in the input plane of a coherent optical Fourier processor. The object specific signatures $P_Q(\phi)$ are obtained by scanning the intehsity in the magnified Fourier spectra $O(\vec{p})$ with a Reticon RO 720 circular photodetector array [5]. Figure 5 shows the four power spectra with the corresponding test objects inserted in the upper right corner. The concentric circles indicate three different scans chosen for signature recording. The radii are equal to 3, 10, and 30 times the mean radius of the zero order spot in the Fourier spectrum, respectively. Since the object functions $O(\vec{x})$ are real-valued, the power spectra are symmetric (Fig.5) and thus the signatures consist of two equal halves. The two halves were superposed to get a shorter signature of better quality. The result was digitized and stored as an array of 360 nine-bit words.

A representative selection of the investigated profiles is shown in Fig.6. They are identified by a code (xYz), where x designates the object (1-4,Fig.5), Y indicates whether the object was displaced (C) or not (A), and z refers to the normalized scan radius (3,10,30) of the circular scan. Reduced angular resolution (< 0.5 deg) or reduced digital resolution of the intensity (< 9 bits) are indicated in parenthesis. As can be seen from the codes, Figs.6a,b,c,e represent equivalent signatures for the four test objects. Figures 2d,e,f show, how the signature structure becomes finer with increasing scan radius. Figure 6h is the same as Fig.6e, but with the object rotated by 45 deg and somewhat shifted. Modified versions of the signature in Fig.6h are shown in the Figs.6g,i. Figure 6g is for reduced angular resolution (2 deg), obtained by averaging over corresponding intervals. Figure 6i is a binary version with the threshold set at the mean value of the intensity.

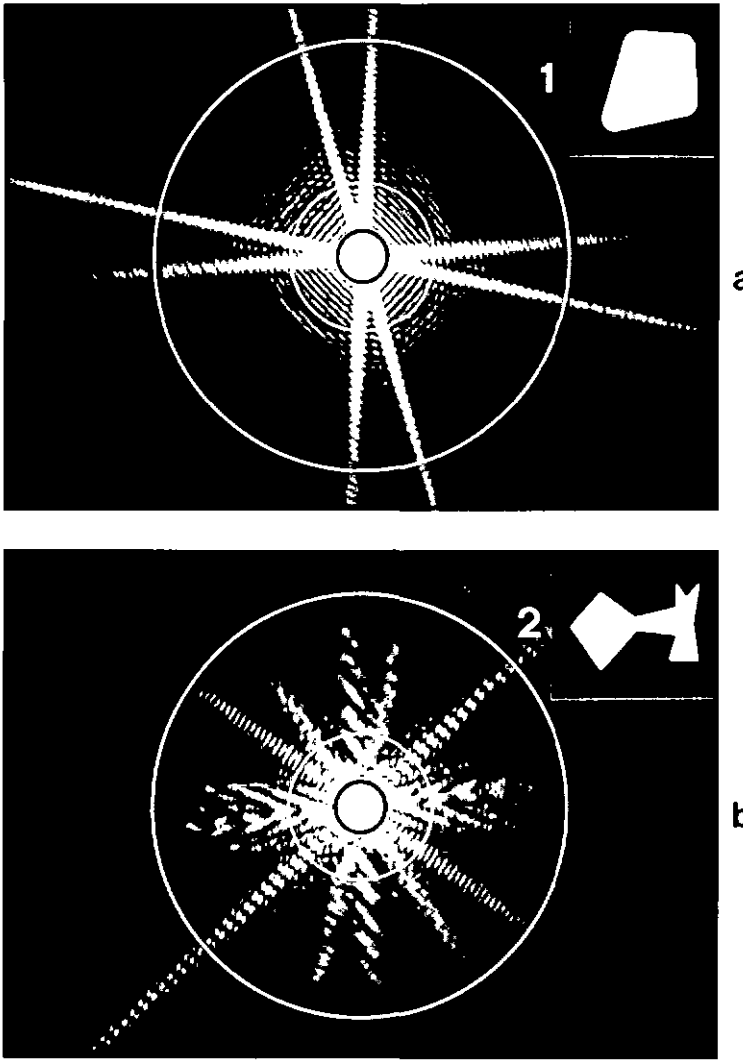

Fig.5 a,b. Power spectra of the test objects shown in the upper right corner. The intensity profiles were scanned along the indicated circles of radii equal to 3, 10 and 30 times the average radius of the zero order diffraction spot, respectively.

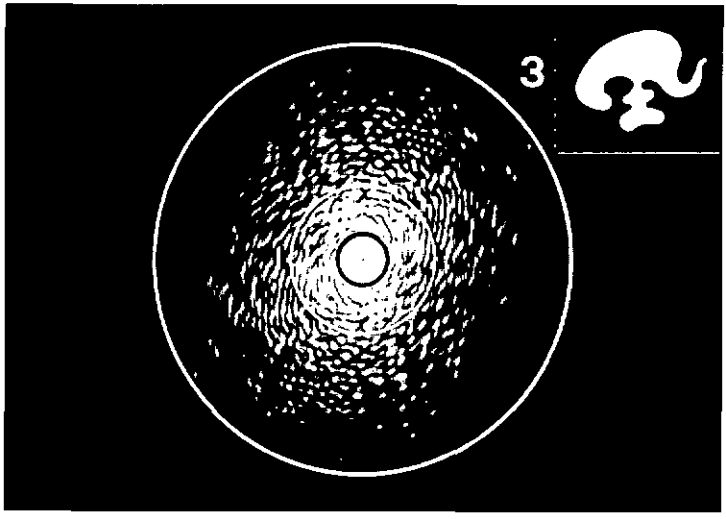

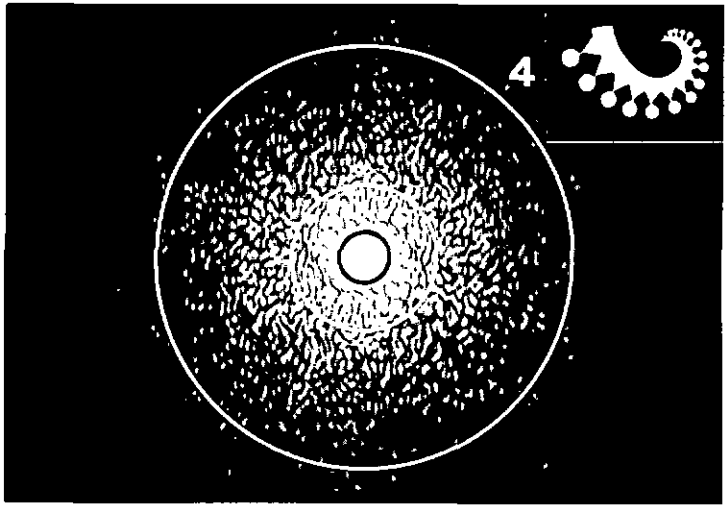

Fig.5 c,d.

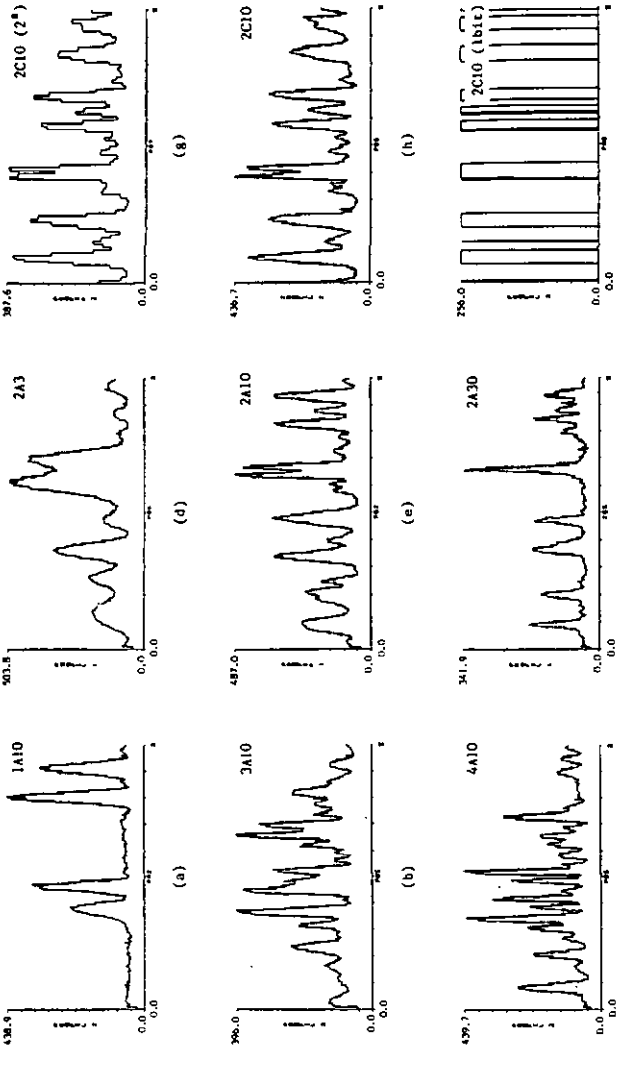

Fig.6. Representative selection of the investigated signatures. The meaning of the codes (e.g.1A10) is explained in the text. (a),(b),(c),(e) show equivalent signatures for the four test objects. (d),(e),(f) correspond to the three circular scans indicated in Fig.5b. (h) is as (e), but for the object rotated and shifted. (g),(i) are modified versions of (h) with reduced angular resolution (2 deg) and binary representation (1 bit), respectively.

The mutual correlations of the profiles were calculated according to Eq.(5) to test the reliability of the object recognition concept. The accuracy of the determination of the object orientation and other important data can be deduced from the correlation functions discussed below. The term "auto-correlation" will be used for convenience when both profiles belong to the same object.

Figure 7 shows some typical examples of the correlation functions and their correlation peaks. The curves are labelled with $C[\alpha,\beta](\gamma)$, where α and β are the signature codes defined above, and γ indicates the angular resolution of the correlation, if different from 0.5 deg (360 points/180 deg). As can be seen from the labels in Fig.7, all curves but the last (f) are auto-correlations, i.e. correlations of profiles belonging to the same object. The object was rotated by 45 deg and somewhat shifted between the two records of the profiles used for the correlations. The profiles are equal to those given in Fig.6, except that they may correspond to different object positions.

The auto-correlations (Figs.7a,b,c) of the signatures in Figs.6f,e,d show the influence of the scan radius: small scan radii yield broad auto-correlation peaks (Fig.7c), as expected from the structure of the power spectrum (Fig.5). Large scan radii yield reduced peak values (Fig.7a), as a result of partial averaging of the power spectrum by the limited angular resolution of the detector array. Figure 7d shows the correlation of the object signature (Fig.6e) with a binary reference signature (Fig.6i). There is no degradation of the correlation peak. Further evidence for the usefulness of binary reference signatures will be given in the next section. A low resolution system has been simmulated by averaging the signatures (Figs.6e,h) over intervals of 2 deg width and calculating the correlation function for 90 arguments spaced at 2 deg (Fig.7e). The intervals were shifted mutually, to avoid averaging over aquivalent sections of the two functions to be correlated. All correlation peak values, except the last one (Fig.7e), are located within 0.5 deg at the nominal value of -45 deg. The accuracy of the determination of the object orientation is therefore approximately given by the angular resolution of the detected signatures. More careful location of the correlation peaks by smoothing the correlation functions in the neighbourhood of the peak values may yield even better results.

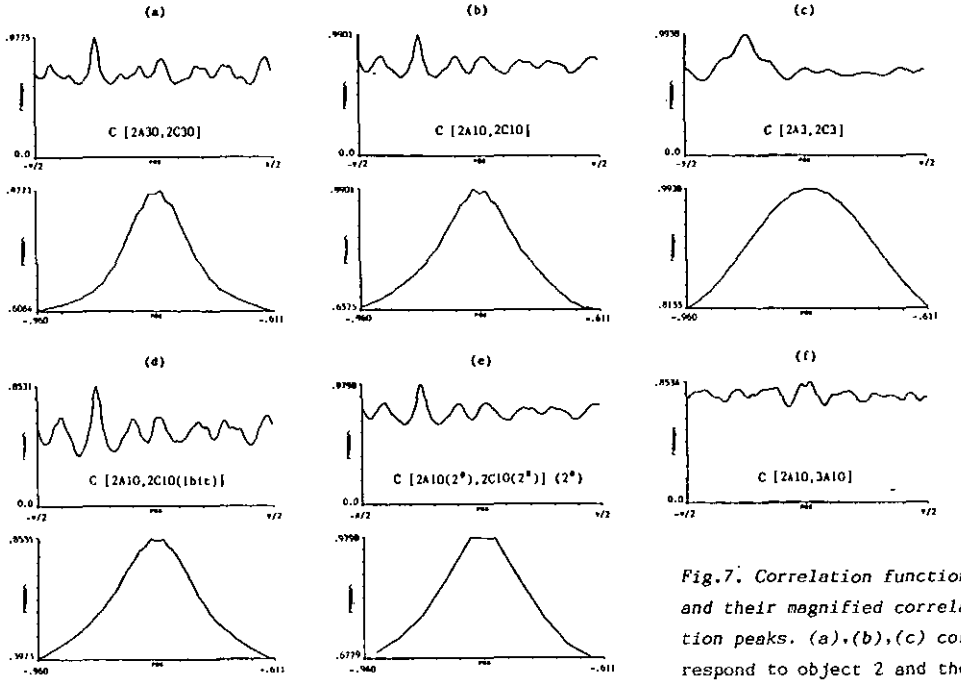

Fig.7. Correlation functions and their magnified correlation peaks. (a),(b),(c) correspond to object 2 and the three different circular scans shown in Fig.5b. (d) is obtained if one of the two signatures is binary. (e) is obtained if both have reduced (2 deg) angular resolution. (f) shows a typical cross-correlation, to be compared with the auto-correlation in (b).

2.1.4 Reliability of object recognition

The reliability of the object discrimination will be discussed in the following. For this purpose correlation functions for various parameters and objects have been calculated and compared. The statistical distribution of peak- and mean-values of the auto- and cross-correlations are shown in Fig.8. Parameters are given where they differ from the standard values, which are: 10 for the normalized scan radius (Fig.5), 0.5 deg for the angular resolution, 9-bit for the signature level representation. The auto-correlation functions have been calculated from three signatures of object 2 (Fig.5b). Two of them correspond to the same object position. Their correlation allows a quantitative estimation of the temporal change of the power spectrum. The third signature belongs to the shifted and rotated object. A decrease of correlelation reflects in this case mainly nonperfect shift invariance, which was found to be far more important than the temporal variations. To get cross-correlations, three additional profiles, representing the objects 1, 3 and 4, have been correlated with a reference profile of object 2 (similar to those shown in Figs.6d-i).

The first three columns of Fig.8 show that increasing the scan radius leads to widely spread mean-values and to reduced peaks of both auto- and cross-correlation functions. This is caused by the partial averaging of the power spectrum due to the limited angular resolution of the detector array and by the reduced reproducibility of the high frequency components of the power spectrum. The data presented in the second section of Fig.8 result from reduced angular resolution. This was simulated by averaging the signatures within N intervals of equal length and calculating the correlation function for N equidistant arguments ($24 \leq N \leq 360$). To avoid averaging over equivalent sections of two signatures belonging to the same object, the intervals were shifted by one half of their width. In this worst case situation, the peak values of the auto-correlations decrease for lower angular resolution (Fig.8). For the cross-correlations, an other effect is dominant. The peak- and the mean-values of the cross-correlations increase as more and more structures, and thus differencies between the profiles, are eliminated due to the reduced resolution. Since the fine structures of the power spectrum are about half the size of the zero order spot, and thus 1/10 the extension of the scan radius, they give rise to about 6 deg wide signature structures. These can be resolved with a minimum angular resolution of 3 deg (60 points/180 deg), according to

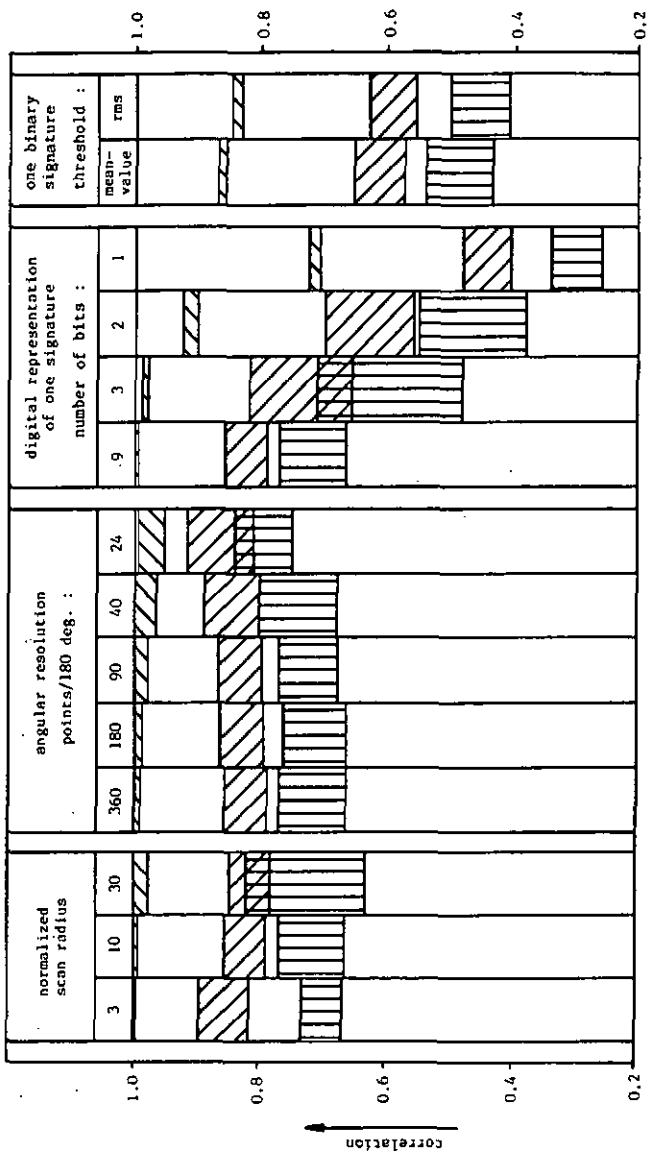

Fig.8. Statistics of peak- and mean-values of auto- and cross-correlations. If not indicated otherwise, the parameters are: normalized scan radius 10, angular resolution 0.5 deg, signature level 9-bit.

the Shannon theorem [6]. Lower resolution leads to considerable signature degradation and thus to smaller differencies between auto- and cross-correlation peak values (Fig.8).

The data represented in the third section of Fig.8 are obtained by reducing the resolution of the level of one of the two signatures to be correlated, i.e. by suppression of the least significant bits. This procedure diminishes the initial similarity between two signatures of the same object and makes the auto-correlation peaks decrease. But the cross-correlation peaks drop even more, so that the difference is still significant and the object can be identified reliably.

The results given in the last three columns of Fig.8 (including one from the third section) were obtained by correlation of an object signature with a binary reference signature. Three different procedures were used to generate these binary functions: The first one consists in considering but the most significant bit of the signature words. The second and third ones use a threshold, equal to the mean value and the root-mean-square of the initial function, respectively. While auto-correlation peak values depend considerably on the binarisation procedure, their separation from the cross-correlation peak values does not. The object discrimination properties are therefore comparable in all three cases.

For maximum reliability of the object identification a threshold has to be set, so that the probability for auto-correlation peaks below and cross-correlation peaks above it is minimal. The optimal parameters and the corresponding threshold level can be determined from the statistical distributions given in Fig.8. However, the statistical data, only 6 correlations per column, are rather poor for this purpose, so far. The development of a dedicated electronic processor will allow to get more data for this purpose. Nevertheless, Fig.8 shows that reliable object recognition is possible for a set of quite different parameters. Unsatisfactory results are only obtained for low angular resolutions, which do not resolve the finest structures of the power spectrum.

2.2 Phase of the spectrum: Object position

2.2.1 Application of the shift theorem

As can be seen from Fig.2, the position of the object centroid is determined from the phase distribution in the Fourier plane. The mathematical base for this procedure is given by the shift theorem. It determines the relation between the Fourier transforms $\hat{O}(\vec{p})$ and $\hat{Q}(\vec{p})$ of two identical but mutually shifted objects $O(\vec{x})$ and $O(\vec{x}-\Delta\vec{x})$:

$$\hat{Q}(\vec{p}) = \hat{O}(\vec{p}) \exp(-i2\pi\Delta\vec{x}\cdot\vec{p}) \quad . \tag{6}$$

Expression (6) shows that an object shift $\Delta\vec{x}$ causes an additional linear phase term $\Delta\psi(\vec{p}) = -2\pi\Delta\vec{x}\cdot\vec{p}$ in the Fourier spectrum. So the linear component of the phase $\psi(\vec{p})$ in the Fourier plane must vanish for one and only one object position. It will be shown (Eq.19) that this position is attained if the centroid of the real-valued object function is on the optical axis. The linear phase component $\psi_s(\vec{p})$ of the spectrum is thus proportional to the position vector $\vec{x}_s$ of the object centroid:

$$\psi_s(\vec{p}) = -2\pi\vec{x}_s\cdot\vec{p} \quad . \tag{7}$$

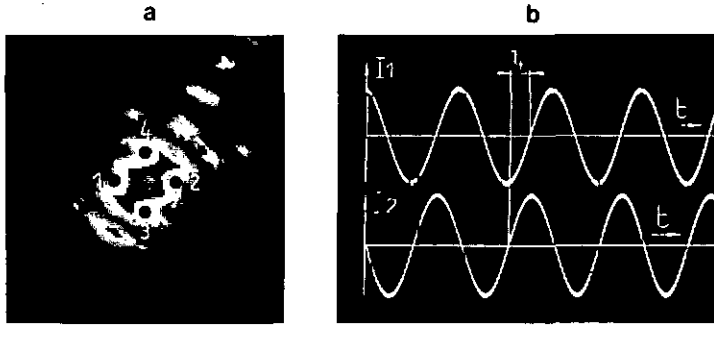

Fig.9. Displacement fringes and phase: (a) detectors in the zero order spot, (b) heterodyne signals for phase measurement.

The detection of $\psi_s(\vec{p})$ by two pairs of photodetectors in the zero order diffraction spot (Fig.9a) yields thus the desired object position $\vec{x}_s$. The phase difference between two opposite detectors, however, must be in the range of ± 180 deg for unambiguous detection of the object position.

The detection of the optical phase requires adequate techniques since no detector is fast enough to respond to the light frequency of about 10^{15} Hz. The basic principle of such methodes is to superpose a reference beam $R(\vec{p})$ to the light field $\hat{Q}(\vec{p})$ to be investigated. The two coherent fields give then rise to an interference pattern (Fig.9a) from which the relative phase of the two complex amplitudes $\hat{Q}(\vec{p})$ and $R(\vec{p})$ can be deduced. The phase distribution in the Fourier spectrum is obtained from this relative phase and the phase of the known reference wave. The precision of the phase retrieval from interference patterns, however, is rather poor ($\approx \lambda/10$). The accurate phase measurements required in the present case were performed with the heterodyne technique [7]. This methode uses a reference wave whose frequency is shifted by $\Delta\omega$ with the help of acoustooptic modulators. The two light waves $\hat{Q}$ and R are thus given by

$$\hat{Q}(t) = |\hat{Q}| \exp[i(\omega t + \psi)] , \tag{8a}$$

$$R(t) = |R| \exp[i((\omega - \Delta\omega)t + \psi_r)] , \tag{8b}$$

where ψ and ψ_r are the phases of the two waves. The superposition of $\hat{Q}(t)$ and R(t) yields a harmonically varying intensity I(t):

$$I(t) = |\hat{Q} + R|^2 = |\hat{Q}|^2 + |R|^2 + \hat{Q}R^* + \hat{Q}^*R$$

$$= |\hat{Q}|^2 + |R|^2 + 2|\hat{Q}||R| \cos(\Delta\omega t + \psi - \psi_r) . \tag{9}$$

If the reference wave is plane and paraxial ($\psi_r(\vec{p})$ = const.), the phase $\psi(\vec{p}) - \psi_r(\vec{p})$ of this intensity modulation shows the same local variation as the phase of the Fourier spectrum $\psi(\vec{p})$. The phase distribution in the Fourier spectrum can thus be determined by detection of the local intensity modulations and electronic measurement of the relative phase shifts. Fig.9b shows the intensity modulations detected at the points 1 and 2 of Fig.9a, ψ is the corresponding phase difference in the Fourier spectrum.

So far, however, the object specific wave front curvature in the zero order diffraction spot has been neglected. It causes an error in the practical measurement of the of the linear phase component because of the finite separation of the detectors. This error can be estimated from the nonlinear phase component $\psi_o(\vec{p})$ representing the wave front curvature. Since the object is real-valued, $\psi_o(\vec{p})$ is an odd function [8]. Two opposite detectors placed at $\vec{p} = \pm \vec{p}_d$ see thus a phase difference of $2\,\psi(\vec{p}_d) \approx 2\,(\psi_s(\vec{p}_d) + \psi_o(\vec{p}_d))$ instead of $2\,\psi_s(\vec{p}_d)$. The relative error in the detection of ψ_s is therefore $\psi_o(\vec{p}_d)/\psi_{smax}(\vec{p}_d)$, where $\psi_{smax}(\vec{p}_d)$ is given by the range of unambiguous phase measurement ($|2\,\psi_{max}(\vec{p}_d)| < 180$ deg). The corresponding error in the determination of the object location is

$$|\Delta x_s|/|x_{smax}| = |\psi_o(\vec{p}_d)|/|90^o - \psi_o(\vec{p}_d)| \quad . \tag{10}$$

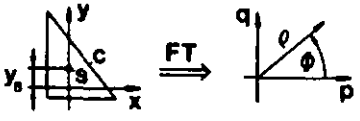

Fig.10. Calculated angular phase variation in the spectrum of a binary triangular object.

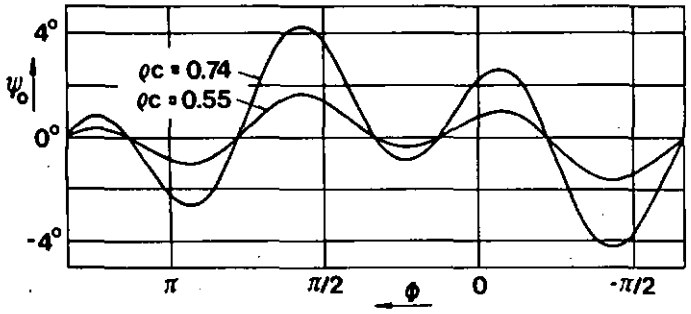

A representative example of a nonlinear phase term in the zero order diffraction spot is given in Fig.10. The curves show the distribution of $\psi_o(\vec{p})$ on two centered circles in the spectrum of a binary triangular object. The corresponding radii are normalized to the object extension c so that $\rho c = 1$ corresponds approximately to the radius of the zero order spot. $\psi_o(\vec{p})$ is less than 2 deg at $\rho c = 0.55$. Thus the object shift $\vec{x}_s$ can be determined to better

than 2% of the maximum allowed object displacement x_{smax} without knowing its angular position or its identification. For closer detector separations, which allow the object to move in a larger field compared to its size, the error caused by ignoring the nonlinear phase term $\psi_o(\vec{p})$ becomes even smaller.

2.2.2 Experimental results

The phase detection in the Fourier spectrum has been tested with an arrangement according to Fig.11. A parallel expanded laser beam is projected on the object mask i.e. a metal plate with a structured opening. The light field behind the mask is then Fourier transformed by a lens (SORL, FX15/5F), so that the spectrum of the object occurs in the back focal plane. A reference beam passes through a pair of acoustooptic modulators which shifts the light frequency by about 40 kHz [7]. This beam is expanded and focused on the Fourier plane where it has the desired plane wave front. The beam waist was chosen to be somewhat larger than the zero order spot of the Fourier spectra. The intensity distribution in the Fourier plane that results from the superposition of the two waves is then imaged onto the detection plane with a magnification of about 200. Two appropriately positioned optical fibers of 75 µm core diameter guide the light to the photomultipliers (RCA 8645). The resulting harmonically modulated electronic signals are bandpass filtered and amplified to match the input conditions of a commercially available phasemeter (EVANS 4119). Careful balancing of the two electrical channels is necessary to avoid additional phase shifts.

The discribed arrangement was first used to experimentally verify the shift theorem (Eq.(6)). For this purpose, a circular object was shifted across the object plane while the phase was detected between two opposite points of the Fourier spectrum. The relation between the object radius R and the detector separation a was chosen to be a = 1/2R, so that the detectors were well inside the zero order spot of the Airy function. Fig.12 shows the analog output ψ of the phasemeter plotted versus the normalized object shift. The estimated error is $\Delta\psi = 1$ deg, which corresponds to an object displacement of $\Delta x_s/R = 0.56\%$. Unambiguous determination of the object position $\vec{x}_s$ requires the measured phase ψ to range within one periode ($|\psi| < 180$ deg), so that the maximum object shift is $x_{smax} = \pm R$ for the chosen detector separation.

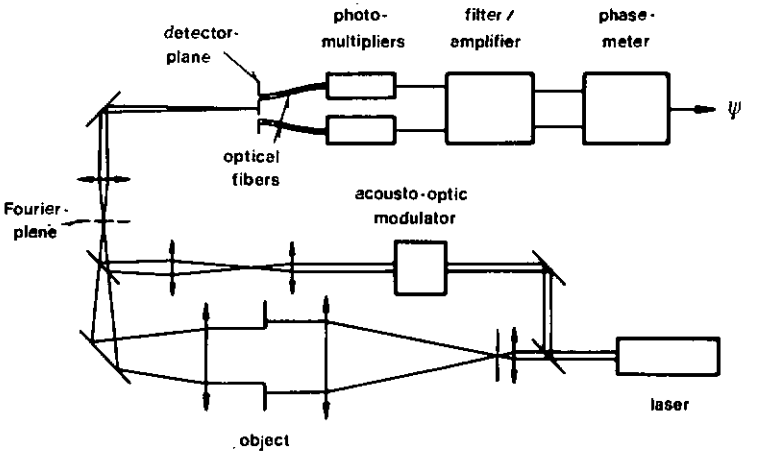

Fig.11. Heterodyne Mach Zehnder interferometer and electronics used for accurate phase measurement in the Fourier spectra.

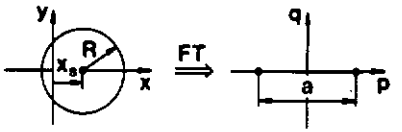

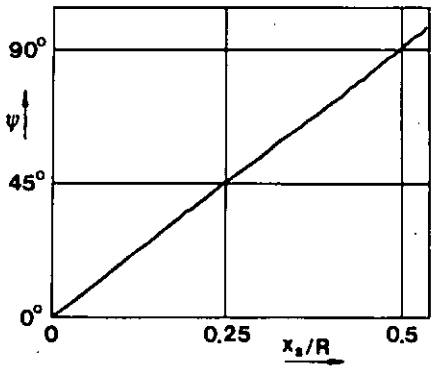

Fig.12. Experimental verification of the shift theorem by heterodyne measurement of the phase ψ. Detector separation is a = 1/2R. Maximum displacement for ψ = ±180 deg is $x_{smax} = \pm R$. The accuracy of the phase measurement is Δψ = 1 deg, the corresponding resolution of the displacement is $\Delta x_s/2R = 0.3\%$.

The used circular object is real-valued and has central symmetry. Thus the Fourier spectrum is real-valued and the wave front in the zero order spot is plane. The linear phase term of the spectrum can be calculated exactly from the signals detected on a finite radius, so that a major error source in the determination of the object position is eliminated. Symmetric objects can therefore be located to better than about 0.3% of the maximum object shift, which corresponds to the relative error in the phase measurement (1 deg/360 deg).

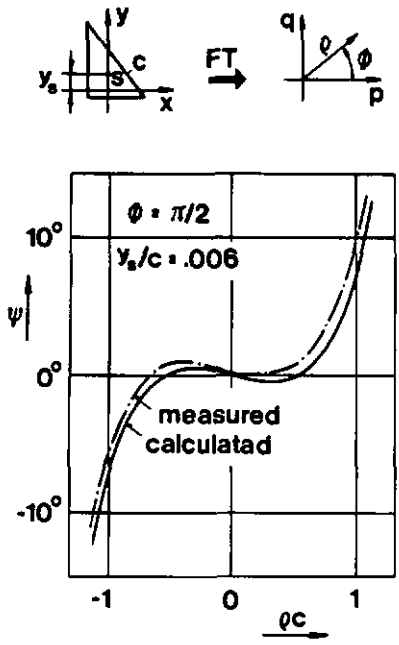

Fig.13. Radial phase distribution in the spectrum of a binary triangular object. The object centroid is only slightly off the optical axis (y_s/c = 0.006), so that the nonlinear object specific phase component becomes prominent.

Real objects without central symmetry yield complex valued hermitian Fourier spectra, i.e. the real component is symmetric, the imaginary component and the phase are asymmetric with respect to the origin [8]. An example of such a phase distribution is given in Fig.13. The curves show the radial phase variation in the Fourier spectrum of a triangular binary object. The radius is normalized to the length of the hypothenuse c of the triangle. The slope of the

curves at $\vec{p} = 0$ reflects a shift y_s between the object centroid and the optical axis. This shift has been chosen to be small compared to the object extension ($y_s/c = 0.006$), so that the related linear term phase term $\psi_s(\vec{p})$ does not dominate the object specific nonlinear phase term $\psi_o(\vec{p})$. Measured and calculated results are consistent within the accuracy of the heterodyne phase detection (1 deg).

Circular scans of the phase $\psi(\rho,\phi)$ in the same spectrum yield the curves shown in Fig.14. The small shift of the object ($x_s/c = 0.0015$, $y_s/c = 0.006$) generates a harmonic term $\psi_s(\phi) = -2\pi\rho(x_s\cos\phi + y_s\sin\phi)$ that represents the difference between the calculated curves in Fig.10 and Fig.14. The outstanding harmonic component with a periode of $2\pi/3$, however, stems from the term of third order in the coordinates p and q, which represents a major part of the object specific phase $\psi_o(\vec{p})$ in the zero order spot. A comparison of the experimental and theoretical results in Fig.14 confirms both the predictions and the accuracy of the heterodyne phase measurement.

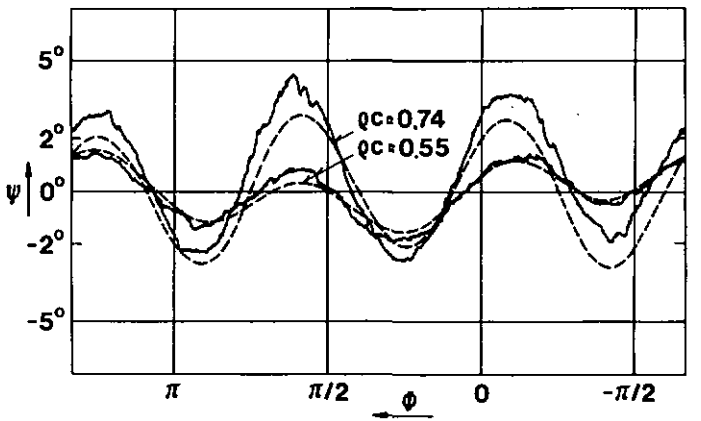

Fig.14. Comparison of calculated (dashed) and measured angular phase variations $\psi(\phi)$ for the same triangle as in Figs.10 and 13.

These experimental results proove that the angular phase variations within the zero order spot $\rho c < 1$ due to wave front curvatures are small compared to the phase caused by an object shift. Typically less than 4 deg of the phase

difference detected by two opposite detectors on the radius $\rho c = 0.55$ result from the curved wave front (Fig.14). This corresponds to about 2% of the phase for maximum object shift (180 deg). Thus the object shift can be determined to better than 2% of the maximum object displacement, as was found from theoretical estimations (sec.2.2.1).

2.2.3 The phase in the zero order spot

The phase distribution within the zero order diffraction spot can be discussed by means of a Taylor expansion of the Fourier spectrum $\hat{Q}(\vec{p})$. This procedure gives insight in the relations between object properties and the resulting spectrum. Such knowlege is necessary for error estimations and for the resolution of the 180 deg ambiguity in the determination of the object orientation. The following discussion of the low order phase terms in the spectrum $\hat{Q}(\vec{p})$ considers both real- and complex-valued objects. The latter can be decomposed in real and imaginary components,

$$Q(\vec{x}) = O(\vec{x}-\vec{x}_s) = A(\vec{x}-\vec{x}_s) + iB(\vec{x}-\vec{x}_s) . \qquad (11)$$

In correspondance with the denomination for real objects, $\vec{x}_s$ has been chosen to give the centroid position of the real component of the object function $Q(\vec{x})$, so that

$$\int \vec{x}\, A(\vec{x})\, d^2x = 0 . \qquad (12)$$

Now the Taylor expansion of the Fourier spectrum $\hat{Q}(\vec{p})$ at $\vec{p} = 0$ reads:

$$\hat{Q}(\vec{p}) = \sum_{j,k} \frac{i}{j!k!} \left[\frac{\partial^{j+k}}{\partial p^j\, \partial q^k} \hat{Q}(\vec{p}) \right]_{\vec{p}=0} p^j\, q^k \qquad (13)$$

The zero order term (j+k=0) in Eq.(13) is equal to the integral of the object function $Q(\vec{x})$ over the object plane.

$$\hat{Q}(0) = \int Q(\vec{x}) \exp(-i2\pi\vec{p}\cdot\vec{x})\, d^2x \Big|_{\vec{p}=0} = \int Q(\vec{x})\, d^2x . \qquad (14)$$

The phase at the origin of the spectrum can be set to zero ($\psi(0) = 0$) without loss of generality. This means that the value of the Fourier transform at the origin is assumed to be real, which is equivalent to the assumption that the mean value of the object function $Q(\vec{x})$ is real (Eq.14):

$$\mathrm{re}\,[\hat{Q}(0)] = \int A(\vec{x}-\vec{x}_s)\, d^2x = \int A(\vec{x})\, d^2x \neq 0 , \qquad (15a)$$

$$\mathrm{im}\,[\hat{Q}(0)] = \int B(\vec{x}-\vec{x}_s)\, d^2x = \int B(\vec{x})\, d^2x = 0 . \qquad (15b)$$

The determination of the linear phase term ψ_s in the Fourier spectrum requires the knowledge of the first order terms of Eq.(13):

$$\vec{p}\cdot[\nabla\hat{Q}(\vec{p})]_{\vec{p}=0} = -i2\pi\vec{p}\int \vec{x}\, Q(\vec{x})\, d^2x$$

$$= -i2\pi\vec{p}\int \vec{x}\, O(\vec{x})\, d^2x - i2\pi\vec{p}\cdot\vec{x}_s\int O(\vec{x})\, d^2x$$

$$= -2\pi\vec{p}\,[i\int \vec{x}\, A(\vec{x})\, d^2x - \int \vec{x}\, B(\vec{x})\, d^2x$$

$$+ i\vec{x}_s\int A(\vec{x})\, d^2x - \vec{x}_s\int B(\vec{x})\, d^2x\,] , \qquad (16)$$

where $\nabla = (\partial/\partial p, \partial/\partial q)$.

The first and the last term in (16) vanish (Eqs.12 and 15b), so that the first order term of $\hat{Q}(\vec{p})$ reads

$$\vec{p}\cdot[\nabla\hat{Q}(\vec{p})]_{\vec{p}=0} = 2\pi\vec{p}\cdot[\int \vec{x}\, B(\vec{x})\, d^2x - i\,\vec{x}_s\cdot\int A(\vec{x})\, d^2x] . \qquad (17)$$

In the neighbourhood of the origin ($\vec{p} = 0$) both the real and the imaginary parts of the spectrum $\hat{Q}(\vec{p})$ can be approximated by the terms of lowest order, which are given by (15a) and (17). The resulting phase $\psi(\vec{p})$ for $\vec{p}\to 0$ is thus

$$\psi(\vec{p})\Big|_{\vec{p}\to 0} = \mathrm{arctg}\,\frac{\mathrm{im}[\hat{Q}(\vec{p})]}{\mathrm{re}[\hat{Q}(\vec{p})]}\Bigg|_{\vec{p}\to 0}$$

$$= \frac{-2\pi\vec{p}\cdot\vec{x}_s\int A(\vec{x})\, d^2x}{\int A(\vec{x})\, d^2x} = -2\pi\vec{p}\cdot\vec{x}_s \qquad (18)$$

Eq.(18) implies that the linear component $\psi_s(\vec{p})$ of the phase $\psi(\vec{p})$ in the Fourier spectrum is given by

$$\psi_s = -2\pi\vec{x}_s\cdot\vec{p} \quad . \tag{19}$$

The relation (19) confirms the shift theorem (Eq.6)) and gives evidence for the above statement (Eq.(7)) saying that the linear phase term $\psi_s(\vec{p})$ in the Fourier spectrum is proportional to the centroid position $\vec{x}_s$ of the real part of the object, if the mean value of the object function is real.

Real-valued object functions yield hermitian Fourier spectra and thus only phase terms of odd order [8]. The linear phase terms vanish for centered objects ($\vec{x}_s = 0$), so that third order terms are dominant near the origin ($\vec{p} \approx 0$). The third order phase approximation can then be deduced from Eq.(13) to be

$$\psi_o(p,q) \approx \psi_3(p,q) = \sum_{j+k=3} \frac{1}{j!k!}\, m_{jk}\, p^j\, q^k \quad , \tag{20}$$

$$\text{where} \quad m_{jk} = -i\,\frac{1}{\hat{Q}(0)}\left[\frac{\partial^{j+k}}{\partial p^j\,\partial q^k}\,\hat{Q}(\vec{p})\right]_{\vec{p}\to 0} \quad , \quad (j+k=3) \quad .$$

In polar coordinates (ρ,ϕ) the approximation (20) becomes, with $p = \rho\cos\phi$ and $q = \rho\sin\phi$, explicitely

$$\psi_3(\rho,\phi) = (\rho/2)^3\,[(m_{30}+m_{12})\cos\phi + (m_{21}+m_{03})\sin\phi + ((m_{30}/3)-m_{12})\cos 3\phi + (m_{21}-(m_{03}/3))\sin 3\phi] \tag{21}$$

This third order approximation (Eqs.20,21) and the exact phase $\psi_o(\rho,\phi)$ are reported in the Figs.15 and 16 for the same triangular object as used in the preceeding Sections. Fig.15 shows the radial distribution and Fig.16 the angular distribution of the phase, respectively.

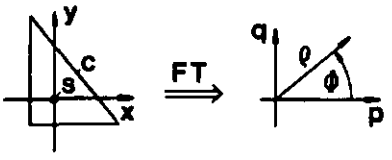

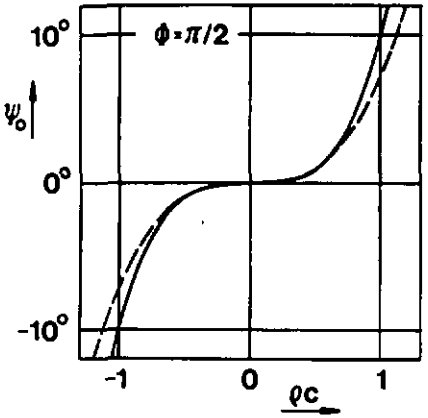

Fig.15. Radial phase variation in the zero order diffraction spot of a triangular object centered on the optical axis ($\vec{x}_s = 0$). Exact values (solid lines) and third order approximations (dashed lines) are given.

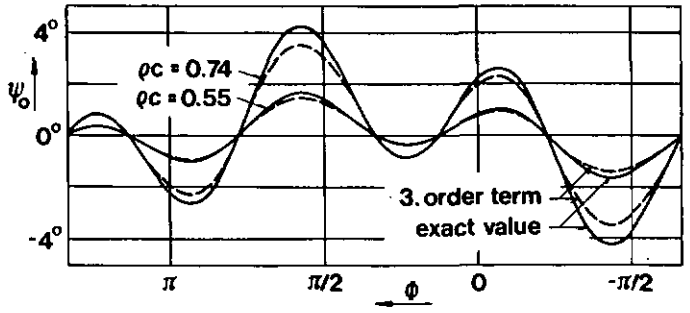

Fig.16. Angular variation of the phase $\psi_0(\phi)$ in the same spectrum as in Fig.15. The dashed curves give the third order approximations.

Note, that a rotation of the object by 180 deg causes an inversion of the sign of the third order phase term in the Fourier spectrum, i.e. $\psi_3(\phi) \approx -\psi_3(\phi+180 \text{ deg})$. The 180 deg ambiguity in the determination of the object orientation (Sec.2.1) can therefore be resolved by looking at the sign of this term. A useful method to resolve this ambiguity with a high immunity to inaccuracies in the detection of the phase term is as follows: The angular distribution of the measured third order phase term $\psi_3(\phi)$ is compared to the reference distribution $\psi r_3(\phi)$ obtained from a learning process with the object at its reference orientation $\alpha = 0$. From the correlation of the circular scan in the power spectrum (Sec.2.1) the angular orientation of the object is known to be $\alpha = \alpha_0$ or α_0+180 deg. The actual object orientation can therefore be determined by checking which angular distribution of the two phase terms, $\psi_3(\phi+\alpha_0)$ or $\psi_3(\phi+\alpha_0+180 \text{ deg})$, is more similar to the reference phase $\psi r_3(\phi)$.

The above comparison is performed most suitably by calculating the value of the cross-correlation

$$C(\phi) = \int_0^{2\pi} \psi_3(\phi') \, \psi r_3(\phi'-\phi) \, d\phi' \qquad (22)$$

for $\phi = \alpha_0$. Since $C(\alpha_0) = -C(\alpha_0+180 \text{ deg})$, $C(\alpha_0) > 0$ indicates that α_0 is the correct object orientation, while $C(\alpha_0) < 0$ is true for the opposite object orientation (α_0+180 deg).

The reliability of this method can be checked by using a normalized version of the correlation function. A useful normaliation is obtained by dividing $C(\phi)$ by C_r, where

$$C_r = \int_0^{2\pi} [\psi r_3(\phi)]^2 \, d\phi \quad . \qquad (23)$$

The values for $C(\alpha_0)/C_r$ and $C(\alpha_0+180 \text{ deg})/C_r$ are ± 1, respectively, for a perfect coincidence between test phase and reference phase. The corresponding values for the general case must not differ too much from unity, otherwise the detected phase terms are not similar to the reference terms and the resolution of the 180 deg ambiguity is not reliable.

The value $C(\alpha_0)$ of the correlation function $C(\phi)$ given in Eq.(22) can be written in terms of the coefficients m_{jk} by using Eq.(21). The integration yields then the explicit result

$$C(\alpha_0) = (1/2) \times \tag{24}$$

$$\{\cos(\alpha_0)\,[(mr_{30}+mr_{12})(m_{30}+m_{12}) + (mr_{21}+mr_{03})(m_{21}+m_{03})]$$

$$+ \sin(\alpha_0)\,[-(mr_{30}+mr_{12})(m_{21}+m_{03}) + (mr_{21}+mr_{03})(m_{30}+m_{12})]$$

$$+ \cos(3\alpha_0)\,[(mr_{30}/3-mr_{12})(m_{30}/3-m_{12}) + (mr_{21}-mr_{03}/3)(m_{21}-m_{03}/3)]$$

$$+ \sin(3\alpha_0)\,[-(mr_{30}/3-mr_{12})(m_{21}/3-m_{03}) + (mr_{21}-mr_{03}/3)(m_{30}-m_{12}/3)]\}\ ,$$

where the mr_{jk} and the m_{jk} correspond to ψr_3 and ψ_3, respectively.

The corresponding expression for the normalisation C_r reads

$$C_r = (1/2)\,\{[(mr_{30}+mr_{12})^2 + (mr_{21}+mr_{03})^2 \tag{25}$$

$$+ (mr_{30}/3-mr_{12})^2 + (mr_{21}-mr_{03}/3)^2]\}\ .$$

It will be shown that the m_{jk} are essentially the third order moments of the object function. The experimental determination of such moments will be extensively discussed in Sec.3. Eqs.(24) and (25) will be used to demonstrate the resolution of the 180 deg ambiguity in the determination of the object orientation by measured object moments.

2.3 Object tracking from one-dimensional images

An alternative to the described object tracking concept based on intensity scanning rather than phase detection is described in this Section. It uses fast coherent optical transformations for the data compression and a microprocessor for the final processing. The basic idea is to form two 1-D images, $P_x(x)$ and $P_y(y)$, of the intensity distribution $I(x,y) = |O(x,y)|^2$ in the object plane by integrating along the x and the y axis, respectively, viz.

$$P_x(x) = \int I(x,y)\, dy \,, \tag{26a}$$

$$P_y(y) = \int I(x,y)\, dx \,. \tag{26b}$$

The centroid coordinates x_s, y_s of the object $I(x,y)$ can then easily be obtained by calculating the centroid locations of the two 1-D images, viz.

$$x_s = \frac{\iint I(x,y)\, x\, dx\, dy}{\iint I(x,y)\, dx\, dy} = \frac{\int P_x(x)\, x\, dx}{\int P_x(x)\, dx} \,, \tag{27a}$$

$$y_s = \frac{\iint I(x,y)\, y\, dx\, dy}{\iint I(x,y)\, dx\, dy} = \frac{\int P_y(y)\, y\, dy}{\int P_y(y)\, dy} \,. \tag{27b}$$

The integration in Eq.(26) is performed by focusing the coherent light from the object plane onto one axis of the image plane, while maintaining the imaging properties along it. The 1-D image is then detected by scanning along the focal line with a linear detector array of sufficient width to collect the focused light (Fig.18). Fig.17 shows the schematic setup of an object recognition system according to Fig.2, but now using the above described principle for the determination of the object position.

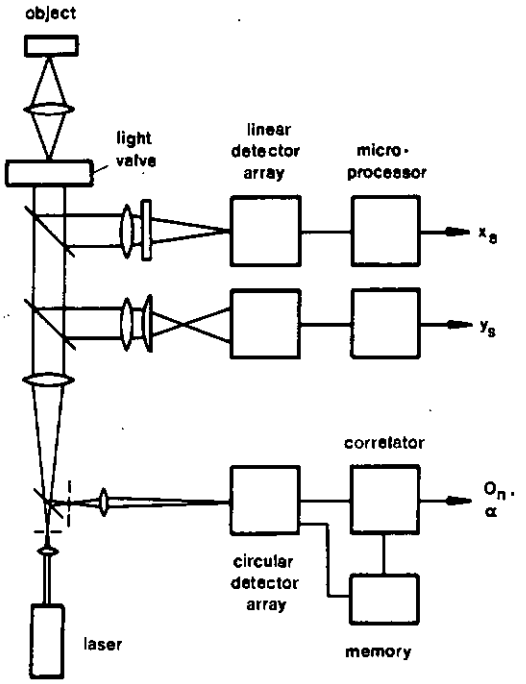

Fig.17. Object recognition system according to Fig.2, but extracting the centroid coordinates of the object from two 1-D images.

2.3.1. One-dimensional optical Fourier transformation

The two astigmatic lens systems in the proposed object tracking concept are designed to perform imaging along one axis and Fourier transformation along the other. This means that for one direction the observation plane is the image plane of the object, whereas for the orthogonal direction the observation plane coincides with the back focal plane of the lens system. Exact optical Fourier transformation requires that the object is located at the front focal plane of the lens system. In the present case, however, the exact position of the object plane is not important, because the associated curvature of the wave front does only affect the phase and not the intensity of the Fourier spectrum.

For the example of focusing onto the y' axis (Fig.18), the amplitude distribution $A_y(x',y')$ in the observation plane is given by

$$A_y(x',y') = (1/g\lambda f)^{1/2} \int O(x,y) \exp(-i2\pi p \cdot x)\, dx \quad , \qquad (28)$$

$$\text{with } p = x'/\lambda f \text{ and } y = -y'/g \quad ,$$

where f is the focal length of the Fourier transform lens and g is the imaging magnification. $A_y(x',y')$ will be called 1-D Fourier spectrum.

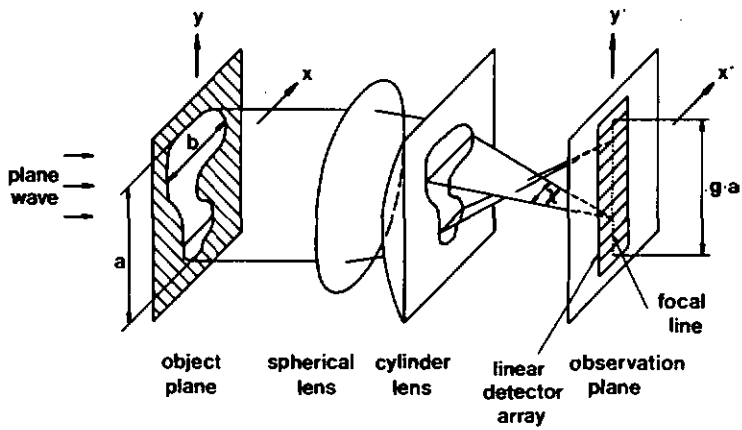

Fig.18. Setup performing one-dimensional Fourier-transformation. A 1-D image $P_{y'}(y')$ of the intensity distribution in the object plane $|O(x,y)|^2$ is scanned by the linear detector array.

Figure 19 shows, as an example, a triangular binary object with its corresponding 1-D Fourier spectrum. The Fourier transform of the one-dimensional amplitude distribution $O(x,y_0)$ for a given y_0 in the object plane is formed at the corresponding $y_0' = -g \cdot y_0$ in the observation plane. For the present binary object the Fourier transform pairs are rect and sinc functions, respectively. Figure 19 shows clearly the inverse proportion between the object width b(y) and the separation of the diffraction fringes.

Note that, for demonstration purpose, the 1-D Fourier transform shown in Fig.19 has been magnified additionally in the x' direction, so that the structure of the spectrum becomes visible.

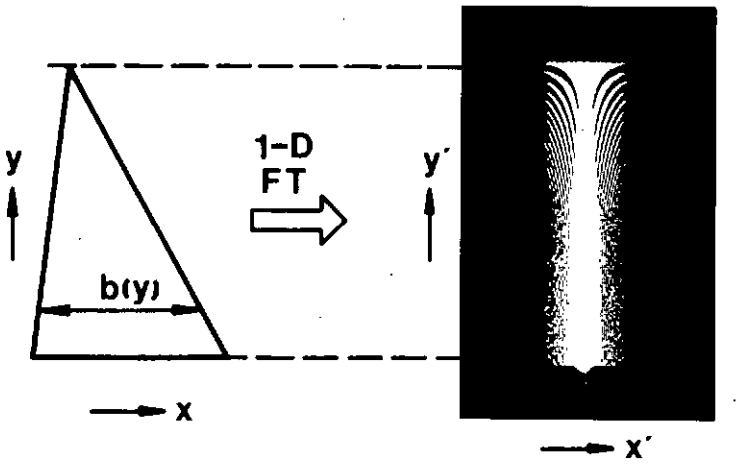

Fig.19. Triangular binary object and its 1-D Fourier spectrum.

From Eq.(28) one finds that the intensity distribution $I_y(x',y')$ in the 1-D spectrum of a binary object with a convex outline is always given by

$$I_y(x',y') = (I_o/g\lambda f)\ |b(y)\ \mathrm{sinc}[b(y)p]|^2$$
$$= (I_o/g\lambda f)\ |\sin[\pi b(y)p]/(\pi p)|^2 \ , \qquad (29)$$

with $p = x'/\lambda f$ and $y = -y'/g$,

where f is the focal length in the x direction (Fig.18), g is the magnification in the y direction, b(y) is the local width (Fig.19) and I_o is the intensity of the object. Objects with concave outlines may yield more complicated intensity distributions, since the cross-sections $O(x,y_0)$ may consist of more than one rectangular function. However, Eq.(29) may still be useful for error discussions.

The combination of an achromatic spherical doublet and a single cylindrical lens (Fig.18) yields a highly astigmatic imaging system with considerable aberrations. But they can be minimized by proper choice of the focal lengths and the relative position of the lenses. A good choice for a system with unit magnification (g = 1) was found to be a spherical lens with f_s = 380 mm and a cylindrical lens with f_c = 300 mm at 48 mm separation. The observation plane, which is also the focal plane of the lens system, is at 381 mm from the spherical lens. Theoretical and experimental results prove that both image distortion and spatial resolution can be made smaller than 0.3% of the object field for an aperture of NA = 0.1 and unit magnification (g = 1). With more elaborate lens systems one could get better imaging quality for even larger apertures. This allows to get narrower 1-D Fourier spectra, which can be scanned by standard detector arrays of limited width (Sec.2.3.2).

2.3.2 Detecting one-dimensional images of two-dimensional objects

The two 1-D images, $P_x(x)$ and $P_y(y)$, for the object tracking (Eqs.(26)) are detected by linear detector arrays of sufficient width to collect all the diffracted light (Fig.18). In practice, however, the width of the available detectors will be limited and the higher diffraction orders (Fig.19) for small object widths b(y) will not be covered. The corresponding errors for the detected power $P_x(x)$ and $P_y(y)$ of the 1-D images and the centroid position will be discussed in the following.

From Eq.(29) one finds for the total integrated power $P_y(y')$ and the fraction $\Delta P_y(y')$ lost due to the limited width d of the detector

$$P_y(y') = 2\int_0^\infty I_y(x',y')\,dx'$$

$$= (2I_o b(y)/g)\int_0^\infty [(\sin\pi a)/(\pi a)]^2\,da = I_o b(y)/g \qquad (30a)$$

$$\Delta P_y(y') = 2\int_{d/2}^\infty I_y(x',y')\,dx'$$

$$= (2I_o b(y)/g)\int_D^\infty [(\sin\pi a)/(\pi a)]^2\,da\ , \qquad (30b)$$

with $D = b(y)d/(2\lambda f)$, and $y = -y'/g$.

Figure 20 shows the ratio $\Delta P_y/P_y$ versus the normalized detector width D in double logarithmic representation. It is seen that the curve oscillates about a straight line. This behavior can be verified by means of the approximation of Eq.(30b) for $D \gg 1$, viz.

$$\begin{aligned} \Delta P_y &= (2I_o b(y)/g) \int_D^\infty [(\sin\pi a/(\pi a)]^2 \, da \\ &\approx (I_o b(y)/g) \int_D^\infty [1/(\pi a)]^2 \, da \\ &= I_o b(y)/(\pi^2 g D) = 2I_o \lambda f/(\pi^2 g d) , \end{aligned} \tag{31}$$

which says that the lost power ΔP_y is independent of the object width b(y), at least as long as $b(y) > (2\lambda f/d)$. This is a consequence of the fact, that the envelope of the 1-D power spectrum is independent of the object width b(y) and the separation of the diffraction fringes (Eq.(29), Fig.19).

The corresponding error of the determination of the object position x_s, y_s can be calculated from Eqs.(27), (30) and (31). For an estimation of this error it is helpful to conclude from Eqs.(30a) and (31) that the loss of the power ΔP_y is essentially equivalent to a reduction of the object width b(y) by a constant amount of $\Delta b = 2\lambda f/\pi^2 d$. Thus the error Δy_s in the detection of y_s due to the loss of the light power ΔP_y is given by the change of y_s, which results from the reduction of the object width b(y) by Δb. Typical values for Δy_s are equal to a fraction of Δb. The same is true for the error in x_s.

A numerical example is given for illustration: For $\lambda = 630$ nm, a detector width of $d = 100$ µm and a focal length of $f = 380$ mm one gets a reduction of the object width of $\Delta b = 0.5$ mm. For a total object field of 50 mm (numerical aperture NA = 0.07) this corresponds to a relative error for the object position of typically less than 1%. In this case the minimum fringe separation in the diffraction pattern (Eq.(29), Fig.19) is found to be 5 µm, so that the detector covers a maximum of $D = 10$ fringe orders and therefore only 1% of the maximum power is lost (Fig.20).

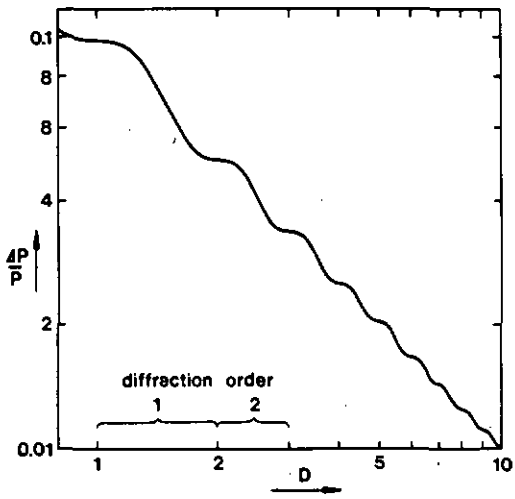

Fig.20. Fraction ΔP/P of light power lost by a detector of finite width d versus the number D of diffraction orders covered by the detector in the sinc pattern.

2.3.3 Error estimation

Two essential sources of error have been discussed already in the preceeding Sections: The aberrations in the 1-D Fourier-transformation and the incomplete one-dimensional integration due to limited detector width. Further errors, which are introduced by the imperfect coherent image of the object, will be discussed in the present Section. This completes the error estimation and gives at the same time a deeper insight into the properties of the object tracking system.

The limited contrast between the bright object and the dark background is another source of error, because the system detects the center of gravity of the whole object field. This error can be calculated from the total light power inside and outside the object, respectively, and from the corresponding centroid positions. A circular binary object covering 10% of the circular object field, for example, can be located to better than 1% of the object field extension, if the contrast is at least 1:300.

Intensity variations across the coherent image of a binary object represent another important source of error. It can be determined by calculating the resulting shift of the object centroid. One-dimensional models are useful for this purpose since they are simple and still representative for the two-dimensional case. A considerable shift of the object centroid can be expected from an additional linear term in the intesity distribution. The corresponding relation between centroid shift and intensity range is given in Fig.21.

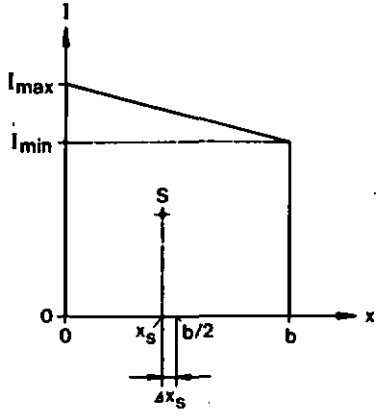

$\frac{I_{max} - I_{min}}{I_{max}}$ [%]	$\frac{\Delta x_s}{b}$ [%]
1	0.084
3	0.25
5	0.42
7	0.60
10	0.88
15	1.35
20	1.85
30	2.94

Fig.21. Linear intensity variation across a 1-D object and resulting shift of the centroid.

The worst case for a given maximum intensity range occurs for a 1-D function which is equal to I_{max} on one side and I_{min} on the other side of the centroid. This intensity distribution yields a centroid shift of $\Delta x_s/b = 4.4\%$ for $(I_{max} - I_{min})/I_{max} = 30\%$. These results show that even considerable intensity variations across the object do not cause serious errors in the determination of the object location. The relative accuracy with respect to the total object field is even better, especially for small objects, since the above values are normalized to the object size.

Wave front distortions introduce important errors in coherent optical processing, when Fourier transformations are involved. They can be reduced by

using expensive high quality optics. The present concept, however, is remarkably insensitive to aberrations. The proof will be given first for wave front curvature in the y-direction and then in the x-direction shown in Fig.18. Wave front curvature in the y-direction does not cause an error as long as the imaging property is maintained (image distortions smaller than 1%) and the light propagation remains inside the aperture of the lens system (angular deviations less than 1 deg). Wave front curvature in the x-direction may affect the details of the Fourier transform pattern. However, since the 1-D image is obtained by integration of the intensity over several diffraction orders, the details and the phase of the Fourier transformation are not important. If the integration covers more than 99% of the maximum power (more than D = 10 orders, Fig.20), wave front distortions as large as 10 λ may be tolerated for the Fourier transformation.

A comparison of this concept with the object tracking methode described in Section 2.2 shows that the first one yields the centroid of the intensity distribution in the object plane (Eq.27), while the second one detects the centroid of the corresponding amplitude distribution (Eq.18). This is a fundamental difference which has considerable influence on the accuracy of the object tracking. The amplitude contrast in the object plane for example, is only the square root of the intensity contrast. The error in the object tracking due to limited contrast is thus much smaller for the present concept. The homogeneity of the object function, however, is better if the amplitude is recognized. The local variations of amplitude and intensity differ by about a factor 2 for the usual case where the intensity varies not more than some 20%. The related error in the object tracking is thus about twice as high for the present concept. Wave front aberrations in the object plane cause errors in the Fourier spectrum, which affects the accuracy of the object tracking described in Section 2.2. The present concept, however, is quite insensitive to such defects, as has been shown above.

2.3.4 Experimental results

The feasibility of the object tracking concept was tested with a setup according to Fig.18. The object mask was illuminated with an expanded parallel beam from a 2 mW He-Ne laser. Since the available linear CCD detector arrays were too narrow (25 µm) for the present aperture of NA = 0.07, the scanning was

performed by a TV-camera and a gated line-integrator. The integration time corresponds to some 3% of the length of a TV line. The light power passing through the object mask was attenuated to about 1 μW to avoid saturation of the camera.

The detected power profiles (1-D images) were digitized and stored as arrays of 625 eight bit words. Since the profile obtained without light could not be adjusted to zero with sufficient accuracy, it was it was compensated by substraction from the detected 1-D images. Such a corrected 1-D image of a binary triangular object is shown in Fig.22.

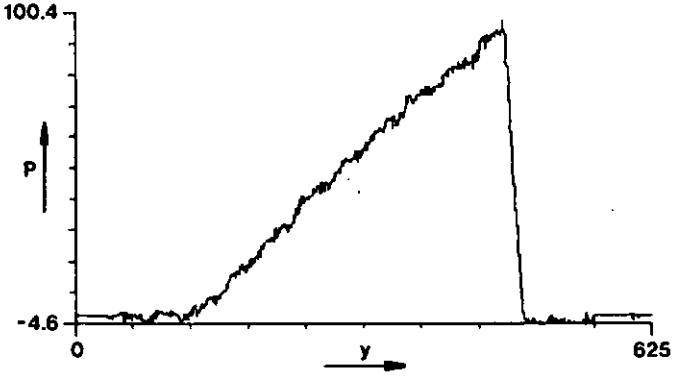

Fig.22. 1-D image (power profile) of a binary triangular object recorded in a setup according to Fig.18.

In order to verify the coincidence of the object centroid and the centroids of the 1-D images, the movement of the latter for a rotation of the object was investigated. A triangular object was rotated in steps of 18 deg. The resulting 1-D images were stored and the position of their centroids calculated. The results are reported in Fig.23. The crosses and the dots belong to two independent series of measurements, respectively. The fitted theoretical harmonic function with a period of 360 deg is shown as solid line. Measured points and fitted theoretical curve differ by less than 4 TV-lines, or 0.6% of the total field length of 625 lines. This deviation is about the same as the difference between the two series of measuements (crosses and dots). There is

evidence that the main cause of this error was the limited temporal stability of the gated line-integrator.

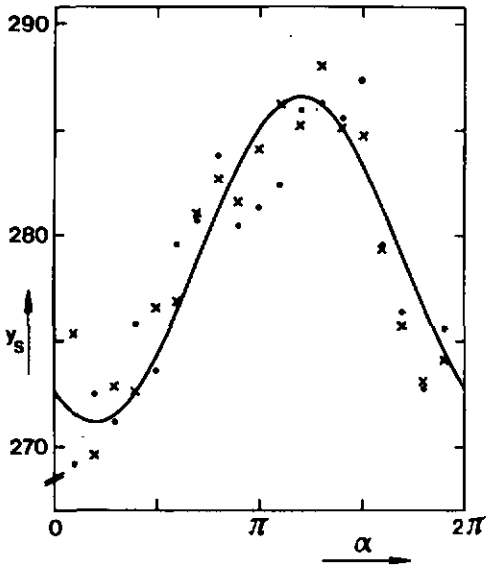

Fig.23. Centroid coordinate y_s of a triangular object versus object rotation, angle α. The crosses and the dots correspond to two independent measurements and the solid line is the fitted theoretical harmonic function.

The described test demonstrates that the detected object location does not depend considerably on the object orientation. In order to verify the linear relation between object displacement and detected object position, a square object (5 mm by 5 mm) was shifted across the object field (35 mm by 35 mm) in steps of about 3 mm. The results are shown in Fig.24. The detected positions differ by less than 4 TV-lines, or about 1% of the maximum object displacement, from the fitted straight line. Further experiments confirmed the results presented in Figs.23 and 24 and thus the feasibilty of the described object tracking concept.

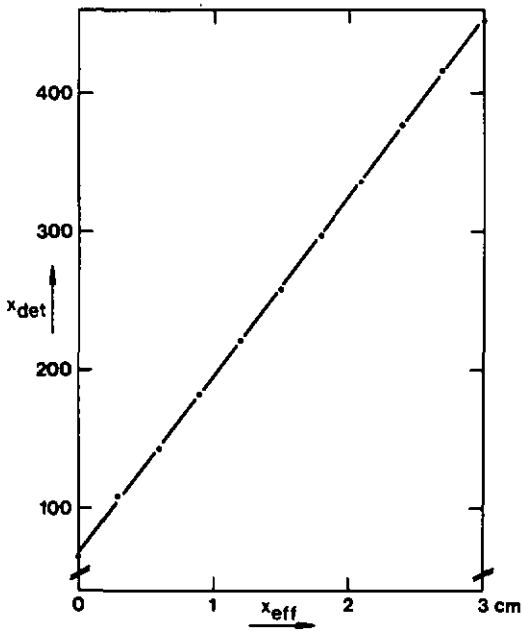

Fig.24. Detected object position x_{det} versus object shift x_{eff} of a 5mm x 5mm square object.

2.4 Conclusion

The hybrid optical-electronic system described in the Sections 2.1 and 2.2 combines the high speed of parallel Fourier processing (coherent optics) and the flexibility of digital programming. This is realized by replacing the matched filter (hardware) in the Fourier plane by electronic processing (software) of amplitude and phase detected in that same plane. The use of this concept in on-line object tracking and recognition has been investigated in detail. The theoretical and experimental results presented give evidence of the feasibility of a hybrid system for industrial robot vision with an incoherent-to-coherent transducer at the input and no moving parts inside, which identifies an object within an ensemble of several (<10) known objects, measures its position to at least 1% accuracy within the field of view, and determines the angular orientation with ~ 1 deg resolution. The response time is expected to be of the order of 0.1 sec; for the time being this is limited by the speed of the image transducer rather than by the electronic and numerical information handling. Learning and programming is easily done by presenting the reference objects at their respective reference positions and electronically memorizing the corresponding signatures and phase values. An iterative approach to the precise object position is possible, using first low resolution at high speed and then gradually increasing the resolution for the correlation and phase determination.

The object tracking described in Section 2.3 is an alternative to the concept presented in Section 2.2. It uses intensity scanning rather than phase detection and offers reduced sensitivity to wave front distortions and contrast limitation in the object plane. The experimental results show, that the location of an object can be determined in about 1 ms to at least 1% accuracy within the field of view. Four 1-D images yield the necessary information on the object asymmetry to resolve the 180 deg ambiguity in the determination of the object orientation (Sec.2.1). Both shape and position of an object can be recognized from a set of several 1-D images as was shown by Radon [9].

3. Object recognition by detection of irradiance moments

3.1. Irradiance moments as classification features

Powerful evaluation of image information is achieved by vision systems which can selectively extract specific features independent from one another. A typical problem is pattern recognition independent of shift, rotation, scale change and inversion. Features like angular orientation, size, or symmetry properties of patterns are often detected for classification or control purposes. In all such cases the determination and evaluation of irradiance moments yields a well suited solution to the problem.

The general method of moments has already been successfully applied for robot vision [10] and aircraft identification [11]. The detection of low order moments of an image is being considered for missile-guidance application and automatic correction of atmospherically degraded telescope images. Moreover it has been shown that the lowest order moments of aerial scene image power spectra are good image quality factors, which can be used as sharpness index for autofocus systems or for contrast measurements [12]. The present work deals with feature extraction and pattern recognition.

The usefulness of the method of moments results from three facts:

- Moments show simple transformation properties when the image is modified by rotation, translation, size change or inversion.
- A unique approximation of an image (or pattern) can be reconstructed from a finite set of moments.
- Low order moments give a rough estimate of a pattern. More details are obtained by including higher order moments.

These properties will be discussed in the following. Fig.25 shows an image plane x,y with a pattern represented as irradiance distribution f(x,y).

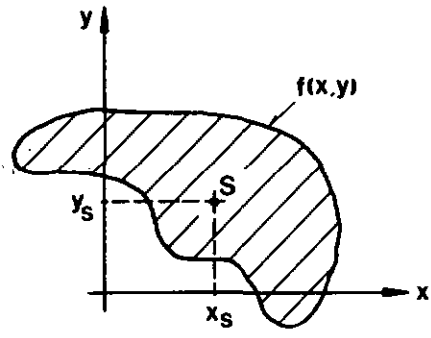

Fig.25. Image plane x,y with pattern discribed by f(x,y).

The usual definition of the moments [8] is

$$M_{jk} = \iint f(x,y)\, x^j\, y^k \, dx\, dy \quad , \tag{32}$$

where the integration is to be performed over the entire image plane. If f(x,y) is a bounded function that has nonzero values only in the finite part of the x,y plane, the moments M_{jk} are uniquely determined. From Eq.(32) one finds that the zero order moment M_{00} represents the total image power

$$M_{00} = \iint f(x,y)\, dx\, dy \quad , \tag{33}$$

while the first order moments give the centroid location x_s, y_s of the irradiance distribution f(x,y)

$$\begin{aligned} M_{10} &= \iint f(x,y)\, x\, dx\, dy = x_s\, M_{00} \, , \\ M_{01} &= \iint f(x,y)\, y\, dx\, dy = y_s\, M_{00} \, . \end{aligned} \tag{34}$$

The second order moments indicate the extension and the orientation of the pattern:

$$\begin{aligned} M_{20} &= \iint f(x,y)\, x^2\, dx\, dy \, , \\ M_{11} &= \iint f(x,y)\, xy\, dx\, dy \, , \end{aligned} \tag{35}$$

$$M_{02} = \iint f(x,y)\, y^2\, dx\, dy \ .$$

Insight in the information content of the higher order moments is obtained by looking at how well an image can be reconstructed from a set of known moments. The second limit theorem of the theory of statistics [13] says that an image can be uniquely reconstructed from all its moments if these are bounded. So one expects that the reconstruction obtained from a limited set of low order moments will resemble the original image. This can be verified by showing that two continuous functions within a limited range with equal moments up to order N have the same least square approximation by a polynomial of order N. The proof will be given for onedimensional functions, but it can easily be extended to the general case. Consider two functions $f^i(x)$, i = 1,2 which have the least square approximations

$$f^i(x) = \sum_{j=0}^{N} a_j^i\, x^j \ , \quad \text{so that}$$

$$\int [f^i(x) - \sum_{j=0}^{N} a_j^i\, x^j]^2\, dx \quad \text{is minimum.} \tag{36}$$

Deriving (36) with respect to a_k^i yields

$$\int f^i(x)\, x^k\, dx = \sum_{j=0}^{N} a_j^i\, x^{j+k}\, dx = M_k^i \ , \quad k = 0...N \tag{37}$$

So if the functions f^1 and f^2 have the same moments ($M_k^1 = M_k^2$, k = 0...N), the approximations are identical ($a_j^1 = a_j^2$, j = 0...N). An original image and the reconstruction have thus the same least square approximation by a polynomial of order N, if they have the moments $M_0 ... M_N$ in common.

The reconstruction of a pattern from a set of low order moments suffers from the drawback that many moments are necessary to obtain a good approximation [14]. However, using the moments as coordinates in a feature space seems quite attractive for pattern recognition. This method consists in characterizing each pattern by a few (n) real numbers that represent the low.

order moments. The n-tuplet of numbers can be considered as an n-dimensional vector pointing somewhere in the feature space. Patterns with equal feature vectors are supposed to be identical. Of course experimentally determined feature vectors will never be exactly reproducible. So one has to find suitable decision rules saying whether a given vector uniquely represents one of the known patterns and which one.

The transformation properties of the moments M_{jk} can be deduced from Eq.(27). A shift of the pattern

$$f(x,y) \rightarrow f'(x,y) = f(x+\Delta x, y+\Delta y)$$

yields the transformed moments

$$M'_{jk} = \sum_{n=0}^{j} \sum_{m=0}^{k} \binom{j}{n}\binom{k}{m} M_{nm}\, \Delta x^{j-n}\, \Delta y^{k-m} \quad . \tag{38}$$

All moments M_{jk} except M_{00} depend on the transverse position of the object (Eq.(38)). The transformed moments are obtained from the original moments of the same and lower order.

A change of the object size according to

$$f(x,y) \rightarrow f''(x,y) = f(x/v, y/v)$$

leads to the transformed moments

$$M''_{jk} = v^{j+k+2}\, M_{jk} \quad . \tag{39}$$

Here the moments are merely multiplied by a factor, which is equal for all moments of the same order.

If the pattern rotates through an angle ϕ, so that

$$f(x,y) \rightarrow f'''(x,y) = f(x\cos\phi - y\sin\phi, x\sin\phi + y\cos\phi) \quad ,$$

the moments change according to

$$M'''_{jk} = \sum_{n=0}^{j} \sum_{m=0}^{k} \binom{j}{n}\binom{k}{m} (-1)^{j-n} M_{n+m,\,j+k-n-m} \times (\cos\phi)^{n+k-m} (\sin\phi)^{j+m-n} \quad . \quad . \qquad (40)$$

As can be seen from Eq.(40), an object rotation makes a set of moments of a given order N = j+k transform into a new set of moments of the same order.

Although the usual definition of moments is given by Eq.(32), there are other useful types of moments. For image reconstruction from known moments for example, one should use "orthogonal" moments to avoid solving coupled systems of equiations [14]. Such orthogonal moments are obtained from the projection of the pattern function f(x,y) onto an orthogonal set of functions rather than on the monomial $x^j y^k$. A typical example are the Legendre moments L_{jk} :

$$L_{jk} = \int\int f(x,y)\, P_j(x)\, P_k(y)\, dx\, dy \quad , \qquad (41)$$

where P_j and P_k are the Legendre polynomials. A suited discription of circular patterns or rotation properties can be achieved using the set of Zernike moments Z_{jk}.

$$Z_{jk} = \int\int f(x,y)\, V_{jk}(\rho,\phi)\, dx\, dy \quad , \qquad (42)$$

where the V_{jk} are the Zernike polynomials [15].

For pattern recognition independent of shift, change of size, rotation and inversion the useful moments are invariant to these geometrical transformations. The application of such invariant moments in pattern recognition was first examined by Hu [16]. Later Dudani [11] established an aircraft recognition system that evaluated 14 low order invariant moments. To his own astonishment this system identified more reliably than four human observers that were well trained to recognize the aircraft models from different points of view.

The object recognition concept discussed in Section 3 uses the same principle of invariant moments. However, the bulk of the computional work is done by optical processing rather than by a digital computer. This way the high computional throughput of parallel optical processors can be applied to speed up the recognition process.

3.2. Invariant moments

In the preceeding Section the utility of invariant moments for pattern recognition was pointed out. A method for the construction of moments which are invariant to shift, change of size, rotation and reflection is discribed in the following.

Translation invariance

The moments M_{jk} are clearly not invariant to a transverse motion of the pattern. However, if the moments are determined with respect to a coordinate system with the origin fixed to a given point of the pattern, they will have the desired property. This reference point is usually chosen to be the centroid of the pattern and the resulting shift invariant moments are called central moments. Thus the central moments m_{jk} are given by

$$m_{jk} = \iint f(x,y)\,(x-x_s)^j\,(y-y_s)^k\,dx\,dy\,, \qquad (43)$$

where x_s and y_s are the centroid coordinates of $f(x,y)$. The m_{jk} are better suited to characterize size and shape of an image pattern than the M_{jk}, since they have no lever arm folded into the numbers. From the Eqs.(32) and (43) one finds the relation between the M_{jk} and the m_{jk}:

$$m_{jk} = \sum_{n=0}^{j}\sum_{m=0}^{k}\binom{j}{n}\binom{k}{m}\,(-x_s)^{j-n}\,(-y_s)^{k-m}\,M_{nm}\,, \qquad (44)$$

where $x_s = M_{10}/M_{00}$ and $y_s = M_{01}/M_{00}$.

Thus the low order central moments are

$$m_{00} = M_{00} \quad , \quad m_{10} = 0 \quad , \quad m_{01} = 0 \quad , \tag{45}$$

$$m_{20} = M_{20} - x_s M_{10} \quad , \quad m_{02} = M_{02} - y_s M_{01} \quad , \quad m_{11} = M_{11} - y_s M_{10} \quad .$$

Note that all moments m_{jk} of odd order j+k are equal to zero if f(x,y) has a center of symmetry.

Scale invariance

If the scale of a pattern f(x,y) changes by a factor v, the new irradiance function is given by

$$f'(x,y) = f(x/v, y/v) \tag{46}$$

and the moments transform according to

$$m'_{jk} = \iint f(x/v, y/v)\, x^j\, y^k \, dx\, dy = v^{2+j+k}\, m_{jk} \quad . \tag{47}$$

Thus the normalized moments

$$\mu'_{jk} = m_{jk} / v^{2+j+k} \tag{48}$$

are invariant to a change of scale. An absolute normalization can be obtained by setting $v = m_{00}^{1/2}$. This yields the shift and size invariant moments

$$\mu_{jk} = m_{jk} / m_{00}^{(j+k+2)/2} \quad . \tag{49}$$

Rotation and reflection invariance

The construction of rotation and reflection invariant moments is more involved. One might think of expressions like

$$E_n = \iint f(x,y)\, (x^2+y^2)^n \, dx\, dy \quad , \tag{50}$$

but Eq.(50) yields only a few of the desired moments. A more rigorous approach was suggested by Hu [16]. He derived rotation and reflection invariant moments from the corresponding transformation rules for the M_{jk}. The simpler method to be discribed here was proposed by Teague [14]. It consists in the use of moments with very simple rotation properties for the construction of invariant linear combinations which can then be expressed by ordinary moments such as the μ_{jk}.

As was mentioned earlier, the definition of moments (32) can by considered as a projection of the pattern $f(x,y)$ on a set of basis vectors $x^j y^k$. The moments M_{jk} have no simple rotation properties (40) since the monomials $x^j y^k$ have not. So one should use a set of basis functions with simple rotation behaviour to define the desired moments. Such a set are the Zernike polinomials V_{jk} [15]

$$V_{jk}(x,y) = V_{jk}(\rho\sin\theta, \rho\cos\theta) = R_{jk}(\rho)\exp(ik\theta) , \qquad (51)$$

where $R_{jk}(\rho)$ is a real valued polynomial of the order j, $j \geq 0$, $|k| \leq j$, and $j-|k|$ = even. These functions are complete over the unit circle and satisfy the relation

$$\iint V_{jk}(x,y)\, V^*_{nm}(x,y)\, dx\, dy = \delta_{jn}\, \delta_{km}\, \pi/(j+1) , \qquad (52)$$

where the integration in (52) is to be performed over the unit disk $x^2+y^2 \leq 1$. Consequently the patterns to be represented are supposed to vanish outside the unit circle. The projection of the pattern function $f(x,y)$ on the Zernike polynomials yields the complex valued Zernike moments Z_{jk}

$$Z_{jk} = \iint f(x,y)\, [V_{jk}(\rho,\theta)]^* dx\, dy . \qquad (53)$$

In the following $f(x,y)$ is considered to be real. In the case of complex valued functions $f(x,y)$, the real and the imaginary parts can be considered seperately, each of them being real. Thus one gets the following relations

$$Z_{jk} = Z^*_{j-k} , \qquad (54)$$

$$Z_{j0} = \text{real} . \qquad (55)$$

The rotation properties of the Zernike moments can be deduced immediately. The irradiance function $f(x,y)$ becomes after rotation through an angle θ_r

$$f''(\rho,\theta) = f(\rho,\theta-\theta_r) \ . \tag{56}$$

This leads to a set of new Zernike moments

$$Z''_{jk} = \iint f(\rho,\theta-\theta_r)\ R_{jk}\ \exp(-ik\theta)\ \rho\ d\rho\ d\theta \ , \tag{57}$$

which satisfy the relation

$$Z''_{jk} = Z_{jk}\ \exp(-ik\theta_r) \ . \tag{58}$$

A reflection of an image across a line through the origin can be decomposed in a reflection across say the y axis and an adequate rotation. Since the moment transformation under image rotation is already known (Eq.(58)), one has to consider but the reflection across the y axis. Such a reflection transforms the original image $f(\rho,\theta)$ into

$$f'''(\rho,\theta) = f(\rho,-\theta) \tag{59}$$

The resulting Zernike moments are

$$Z'''_{jk} = \iint f(\rho,-\theta)\ R_{jk}\ \exp(-ik\theta)\ \rho\ d\rho\ d\theta \ , \tag{60}$$

and the tranformation of the moments reads

$$Z'''_{jk} = Z^*_{jk} \ . \tag{61}$$

In order to construct rotation and reflection invariant moments, one has to find linear combinations of the Z_{jk}, which remain unchanged under the transformations (58) and (61). The expressions Z_{00} and $|Z_{11}|$ are the first invariants, but they become trivial (independent of the pattern (Eq.(66))) through normalisation to shift and size. The second order Zernike moments Z_{22}, Z_{20}, Z_{2-2} generate the invariants

$$\phi_1' = Z_{20} \ ,$$
$$\phi_2' = |Z_{22}|^2 = |Z_{2-2}|^2 \ . \tag{62a}$$

Further invariants are obtained by including the third order moments Z_{30}, Z_{31}, Z_{3-1}, Z_{3-3}. They read

$$\phi_3' = |Z_{31}|^2 \ ,$$
$$\phi_4' = |Z_{33}|^2 \ ,$$
$$\phi_5' = Z_{33}\,(Z_{31}^*)^3 + [Z_{33}\,(Z_{31}^*)^3]^* \ , \tag{62b}$$
$$\phi_6' = Z_{31}^2\,Z_{22}^* + (Z_{31}^2\,Z_{22}^*)^* \ .$$

No further independent invariants can be constructed from the Zernike moments up to order three. This is seen by comparing the number of generating and generated functions. If these were equal, one could solve for the Zernike moments from the known invariants. But this is not possible since the Zernike moments carry the information on angular position and reflection while the invariants do not. The eight invariants $(\phi_1' \ldots \phi_6', Z_{00}, |Z_{11}|^2)$ plus the two informations on angular position and reflection will uniquely determine the ten Zernike moments up to order three, which means that there are no more independent invariant moments of order three or less.

Since it is convenient to have the invariants expressed by ordinary moments, one establishes the relation between the Z_{jk} and the M_{jk}. From the definition of the Zernike moments (Eqs.(51),(53)) and the expression

$$R_{jk}(\rho) = \sum_{n=k}^{j} A_{jkn}\,\rho^n \tag{63}$$

for the radial polynomials of the Zernike functions one gets

$$Z_{jk} = \sum_{n=k}^{j} \sum_{m=0}^{q} \sum_{p=0}^{k} \binom{q}{m} \binom{k}{p} (-i)^p A_{jkn} M_{n-2m-k+p,2m+k-p} , \qquad (64)$$

where $q = (n-k/2)$.

Equation (64) still holds, if the moment generating pattern function $f(x,y)$ is centered ($x_s, y_s = 0$) and normalized in size ($M_{00} = 1$). In this condition the moments M_{jk} are equal to the central moments μ_{jk} (Eq.(49)) and analogously the Z_{jk} will be called z_{jk}. Eq.(64) reads then

$$z_{jk} = \sum_{n=k}^{j} \sum_{m=0}^{q} \sum_{p=0}^{k} \binom{q}{m} \binom{k}{p} (-i)^p A_{jkn} \mu_{n-2m-k+p,2m+k-p} . \qquad (65)$$

Some special cases of Eq.(65) are quoted for later use:

$$\begin{aligned}
z_{00} &= \mu_{00} = 1 \\
z_{11} &= 0 \\
z_{20} &= 2\mu_{20} + 2\mu_{02} - 1 \\
z_{22} &= \mu_{02} - \mu_{20} - i2\mu_{11} \\
z_{31} &= 3\,[(\mu_{03} + \mu_{21}) - i(\mu_{30} + \mu_{12})] \\
z_{33} &= (\mu_{03} - 3\mu_{21}) + i(\mu_{30} - 3\mu_{12})
\end{aligned} \qquad (66)$$

The moments z_{jk} are shift- and size-invariant like the μ_{jk}, but have the same rotation and reflection behaviour as the Z_{jk}, since they form a sub-group of the latter. Thus they can be combined following Eq.(62) to yield moments ϕ_i, which are invariant with respect to shift, change of scale, rotation and reflection. With Eq.(66) one obtains

$$\phi_1 = \mu_{20} + \mu_{02}$$

$$\phi_2 = (\mu_{20} - \mu_{02})^2 + 4\mu_{11}^2$$

$$\phi_3 = (\mu_{03} + \mu_{21})^2 + (\mu_{30} + \mu_{12})^2 \qquad (67)$$

$$\phi_4 = (\mu_{03} - 3\mu_{21})^2 + (\mu_{30} - 3\mu_{12})^2$$

$$\phi_5 = (\mu_{03} - 3\mu_{21})(\mu_{03} + \mu_{21})\,[(\mu_{03} + \mu_{21})^2 - 3(\mu_{30} + \mu_{12})^2]$$
$$+ (\mu_{30} - 3\mu_{12})(\mu_{30} + \mu_{12})\,[(\mu_{30} + \mu_{12})^2 - 3(\mu_{03} + \mu_{21})^2]$$

$$\phi_6 = (\mu_{02} - \mu_{20})\,[(\mu_{03} + \mu_{21})^2 - (\mu_{30} + \mu_{12})^2]$$
$$+ 4\mu_{11}(\mu_{03} + \mu_{21})(\mu_{30} + \mu_{12})\,.$$

These expressions (67) are identical to those derived by Hu [16].

3.3. Detection of irradiance moments

Irradiance moments are usually determined through evaluation of video signals by digital computers [11,16]. But this method suffers from quantisation errors and slow serial processing. Novel concepts using parallel coherent optical processors with holographic filters in the object plane were proposed to circumvent these drawbacks [17,18]. However, the generation of the complicated filters with sufficient accuracy is not trivial. Hybrid opto-electronical systems, which determine irradiance moments by electronic evaluation of the sampled Fourier spectrum were put forward by Fercher [19] and Teague [20]. The concept of Fercher allows the detection of the moments of the autocorrelation rather than those of the pattern itself, because it looks only at the intensity distribution of the complex spectrum. The method of Teague would probably cause serious stability problems in practical realisation and it uses an inadequate sampling procedure (see 3.4.2). The concept to be described in the following applies the same basic principles, but improved techniques to feasibly determine the irradiance moments of an input pattern.

Moment theorem

The mathematical base of the approach is given by the moment theorem [21]. It denotes the relation between the Fourier spectrum $F(p,q)$ and the irradiance moments M_{jk} of a pattern $f(x,y)$. From the definitions

$$M_{jk} = \iint f(x,y)\, x^j\, y^k \, dx\, dy \qquad \text{and}$$

$$F(p,q) = \iint f(x,y)\, \exp[-i2\pi(px+qy)]\, dxdy$$

it is straight forward to derive the moment theorem

$$M_{jk} = [1/(-i2\pi)^{j+k}] \left[(\frac{\partial}{\partial p})^j\, (\frac{\partial}{\partial q})^k\, F(p,q) \right]_{p=q=0} . \qquad (68)$$

Equation (68) says that the moments M_{jk} are given by the derivatives of the spectrum $F(p,q)$ at the origin. These derivatives can be determined by placing a 2-D detector array in the spectrum and by evaluating the samples appropriately. Insight in the relation between the sampled data and the retrievable moments is given by the inverse formula of Eq.(68)

$$F(p,q) = \sum_{j=0}^{\infty} \sum_{k=0}^{\infty} (-i2\pi)^{j+k} (1/j!k!) M_{jk} p^j q^k \quad . \qquad (69)$$

Equation (69) shows that the moments M_{jk} are essentially the expansion terms of the Taylor approximation of $F(p,q)$ at the origin. So, given the set of moments M_{jk} up to order n, one knows the Taylor expansion of F to the n^{th} order (F_n) and vice versa.

If the object centroid is located at the origin, the moments M_{jk} are identical to the central moments m_{jk}. The Taylor expansion of the corresponding Fourier spectrum F_0 can then be written as

$$F_0(p,q) = \sum_{j=0}^{\infty} \sum_{k=0}^{\infty} (-i2\pi)^{j+k} (1/j!k!) m_{jk} p^j q^k \quad . \qquad (70)$$

Intensity sampling

The complex valued spectrum $F(p,q)$ can not be sampled simply by placing a detector array in the Fourier plane. But the power spectrum $|F(p,q)|^2$ sampled by such a set-up contains already useful information on the object moments. This can be checked by looking at the Taylor expansion of $|F(p,q)|^2$. It should be noted that the power spectrum is rather determined by the central moments m_{jk} than by the M_{jk}, since $|F|^2$ is shift invariant. Equation (71) denotes the Taylor expansion of $|F|^2$ up to the fourth order in terms of the central moments m_{jk} for a real valued object function.

Equation (71) contains only terms of even order, since the real valued object has a hermitian Fourier spectrum and thus a symmetric power spectrum. The expression contains 9 monomial expansion terms and 9 central moments m_{jk}. These moments can therefore be retrieved from the known Taylor expansion of $|F|^2$. The expansion terms of sixth and higher order contain moments of both even and odd order, so that there are more unknown moments than known expansion terms. Thus the 9 central moments of order 0, 2 and 4 can be detected by sampling the power spectrum, if the object function is real valued.

$$|F(p,q)|^2 = m_{00}^2 - 4\pi^2 [m_{00}(p^2 m_{20} + 2pq m_{11} + q^2 m_{02})] \qquad (71)$$

$$+ 4\pi^4/3 [p^4(m_{00}m_{40} + 3m_{20}^2) + p^3 q(4m_{00}m_{31} + 12m_{11}m_{20})$$

$$+ p^2 q^2(6m_{00}m_{22} + 6m_{20}m_{02} + 12m_{11}^2) + pq^3(4m_{00}m_{13} + 12m_{11}m_{02})$$

$$+ q^4(m_{00}m_{04} + 3m_{02}^2)] + \ldots$$

A coarse estimation of the accuracy will be given for the example of the detection of m_{20}. The Taylor expansion of the power spectrum on the p-axis can be written as

$$|F(p,0)|^2 = I(p) = I_0 - 4\pi^2 p^2 m_{00} m_{20} + \ldots \qquad (72)$$

From Eq.(72) one gets

$$m_{20} \simeq \frac{I_0 - I(p)}{4\pi^2 p^2 m_{00}} , \qquad (73)$$

and the relative error of the detected moment m_{20} is given by

$$\frac{\Delta m_{20}}{m_{20}} \simeq \frac{\Delta(I_0 - I(p))}{I_0 - I(p)} . \qquad (74)$$

A quantitative estimation can be obtained with the help of Fig.26, which shows $|F(p,0)|^2$ for a triangular object. The spatial frequency p is normalized with respect to the length c of the hypothenuse of the triangle. Figure 26 shows clearly, that the accuracy of the Taylor approximations of different order depend strongly on the the maximum value pc taken into account. Using only second order terms, pc = 0.5 may be an acceptable compromise between this systematic error, which increases with pc and the measuring error (Eq.(74)), which decreases with with pc. Assuming a relative error of $\Delta I/I_0$ = 1% for the detection of the intensities I_0 and I(p), and using I(pc) given in Fig.26 with pc = 0.5 for the sample spacing, one gets from Eq.(74) a relative error of $\Delta m_{20}/m_{20}$ = 6%.

This error results only from the limited accuracy of the intensity measurement. The neglegtion of the Taylor expansion terms of order four and higher (Eq.(72)) causes another error of 11% in the present example. For larger sample spacings pc the first error is reduced, but the second is increased, and vice versa. The second error can be reduced considerably by increasing the number of samples and taking account of the fourth order expansion terms.

The above estimation shows that it is not trivial to detect the second order moments to better than 10%. The detection of fourth order moments is even more difficult. An extensive discussion of additional sources of error will be given in Section 3.4, in connection with the extraction of third order moments from the sampled phase.

Phase sampling

Useful methods to detect the phase $\psi(p,q)$ in the Fourier spectrum will be discussed in Section 3.4.1. The present Section deals with the question of which moments can be calculated from the sampled phase distribution. The answer is obtained from the Taylor expansion of $\psi(p,q)$, whose coefficients are essentially linear combinations of the object moments. A useful representation is found by looking at the shift theorem. This theorem says that $\psi(p,q)$ consists of a shift variant linear term and a shift invariant component. The first term is proportional to the centroid coordinates x_s, y_s of the object function. The latter is equal to $\psi(p,q)$ if the object centroid is at the origin, it is therefore given by the central moments m_{jk}.

An adequate representation of the Taylor expansion of $\psi(p,q)$ is thus obtained, if the coefficients are expressed by x_s, y_s and the m_{jk}. Equation (75) gives the expansion terms up to order 3 for a real valued object function.

$$\psi(p,q) = -2\pi (x_s p + y_s q) \qquad (75)$$

$$+ (4\pi^3/3m_{00})(m_{30}p^3 + 3m_{21}p^2q + 3m_{12}pq^2 + m_{03}q^3) + \ldots$$

A study of Eq.(75) shows that the object position x_s, y_s and the central moments of order three can be deduced from the sampled phase $\psi(p,q)$, if the zero order moment m_{00} is known. The expansion terms of fifth and higher order

contain moments of both even and odd order and one can therefore not solve for the moments.

$\Psi(p,q)$ is an odd function, since the real valued object has a hermitian Fourier spectrum. The first term in Eq.(75) vanishes, if the object centroid is situated at the origin. The second (third order) term gives an approximate discription of the object shape. Note, however, that the central moments of odd order vanish, if the object has central symmetry. So, in this case, the third order phase term is equal to zero.

Conclusion: By sampling the phase in the Fourier spectrum of a real valued object function, the centroid coordinates x_s, y_s and the central moments of order three can be detected, if m_{00} is known.

Useful sampling domain

It is evident, that any number of moments can be determined, if both intensity and phase of a Fourier spectrum are known. Adequate sampling schemes and the evaluation will be extensively discussed in the Sections 3.4.2 and 3.4.3. In the following it will be shown which domain of the spectrum must be sampled, if some low order moments are to be deduced from a small number of samples. For this purpose one recalls that all moments M_{jk} up to order n are given by the Taylor approximation of the n^{th} order F_n (Eq.(69)). F_n can be determined approximately by sampling F in the domain where F and F_n are essentially identical. In a larger sampling area the terms of order n+1 and higher are too important to be neglected. Samples taken in too small an area do not depend significantly on the expansion terms of order n, n-1, etc., so that they are not detected with sufficient accuracy. Thus, one has to compare the Taylor approximation F_n with the spectrum F to find the suitable sampling domain. An idea of the behaviour of such functions is given by Fig.26. It shows radial scans of the real and the imaginary part, the intensity and the phase through the spectrum of a binary rectangular triangle together with the Taylor approximations up to order seven. None of the approximations fits the exact curve well outside the zero order diffraction spot ($\rho c > 1.5$). The adequate sampling domain is thus smaller than this spot for the detection of moments up to order seven.

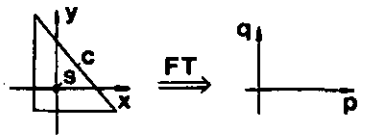

Fig.26. Radial scans of real and imaginary part Re and Im, respectively, as well as intensity I and phase ψ in the Fourier spectrum of a binary rectangular triangle. Exact values and Taylor approximations up to order 7 are denoted by e,2,3,4,5,6,7.

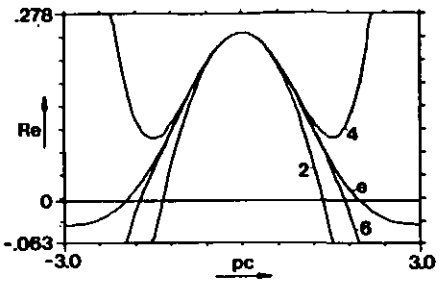

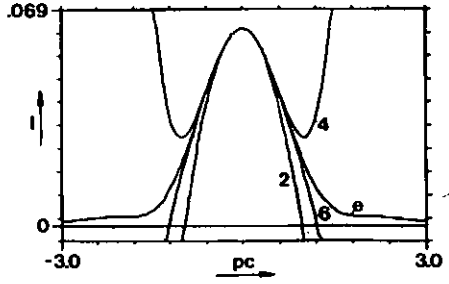

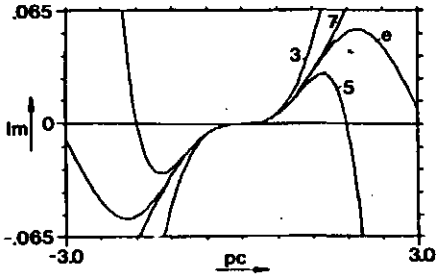

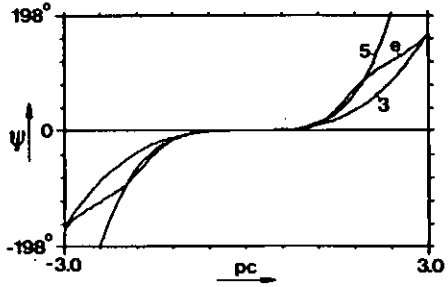

3.4 Moment retrieval from the phase of the Fourier spectrum

Most reliable pattern recognition is obtained, if the pattern are characterized by a considerable number (say 20) of low order irradiance moments. It has been shown in Section 3.3, that this requires both phase and intensity to be sampled in the Fourier spectrum. An elegant method to do this sampling is offered by the digital interferometry technique [22] discribed in the next Section. However, it is not trivial to detect the phase with the required accuracy of better than 1 deg ($\lambda/360$) by means of this method. The feasibility of the moment detection concept will therefore be tested by sampling but the phase of the Fourier spectrum, which can be measured accurately by the heterodyne method [7]. Problems concerning sampling and evaluation remain essentially unchanged by this restriction to phase only detection. The results will therefore be largely representative for combined phase and intensity sampling.

3.4.1 Detection of the optical phase

The phase of a light wave can not be determined by detecting the oscillation of the electromagnetic field, since no detector is fast enough to respond to the light frequency of some 10^{15} Hz. By interferometric techniques, however, it is possible to detect the local variation of the phase. For this purpose a known reference beam

$$R(x,y,t) = |R| \exp[i(\omega t + \psi_r(x,y))]$$

is superposed to the light field

$$O(x,y,t) = |O| \exp[i(\omega t + \psi(x,y))]$$

to be investigated. The two waves give then rise to an interference pattern

$$I(x,y) = |R+O|^2 = |R|^2+|O|^2+ 2|O||R|\cos[\psi(x,y)-\psi_r(x,y)] , \qquad (76)$$

from which the phase difference $\psi-\psi_r$ can be determined. ψ is thus, like ψ_r, given exept for a constant bias term. The accuracy of the phase retrieval from interference patterns is rather poor ($\approx\lambda/10$). More accurate methods are discribed in the following.

Digital interferometry

A smart approach to measure the phase and intensity simultaneously was proposed by Bruning et al. [23]. This method is called digital interferometry or quasi-heterodyne interferometry. It uses a reference wave R whose phase ψ_r is shifted in a controlled manner by a moving mirror or by an electrooptical device. The resulting temporally varying intensity distribution is then sampled by a detector array and evaluated by a microprocessor. The concept allows phase measurements with an accuracy of about $\lambda/100$ [24]. Optical aberrations in the test system can be compensated by adequate software.

In the four step technique the reference phase ψ_r is shifted in steps of $\pi/2$. This causes the intensity to assume successively four values at each point of the detection plane. Equation (76) shows that the four intensity levels, which correspond to $\psi_r = 0, \pi/2, \pi, 3\pi/2$, respectively, can be expressed as

$$\begin{aligned} I_1(x,y) &= A(x,y) + B(x,y)\cos[\psi(x,y)] , \\ I_2(x,y) &= A(x,y) + B(x,y)\sin[\psi(x,y)] , \\ I_3(x,y) &= A(x,y) - B(x,y)\cos[\psi(x,y)] , \\ I_4(x,y) &= A(x,y) - B(x,y)\sin[\psi(x,y)] . \end{aligned} \tag{77}$$

Solving Eqs.(77) for ψ yields

$$\psi(x,y) = \operatorname{artg} \frac{I_2(x,y) - I_4(x,y)}{I_1(x,y) - I_3(x,y)} . \tag{78}$$

The phase can thus be determined for each detector element individually. Intensity variations across the detector array are compensated due to the division and substraction in Eq.(78). Evidently the unknown A and B, and thus $|O|$ and $|R|$, can also be deduced from the four intensities $I_1 \ldots I_4$. Note that A, B, and ψ can be determined in a similar way using only three steps. The four step method has been discribed for simplicity.

In the integrating bucket technique the phase ψ_r of the reference wave is a linear function of time [22]. Each detector element integrates the resulting intensity over a certain time interval before it is read out. For example in the three bucket technique the detector is read out every time the phase has changed by $\pi/2$. The detected values for the phase intervals ψ_r = $0-\pi/2$, $\pi/2-\pi$, $\pi-3\pi/2$ can be written as

$$P_1(x,y) = C(x,y) + D(x,y)[-\cos\psi(x,y)-\sin\psi(x,y)]$$

$$P_2(x,y) = C(x,y) + D(x,y)[\cos\psi(x,y)-\sin\psi(x,y)] \qquad (79)$$

$$P_3(x,y) = C(x,y) + D(x,y)[\cos\psi(x,y)+\sin\psi(x,y)] \ .$$

It follows from Eq.(79), that the phase ψ is obtained from

$$\psi(x,y) = \text{artg}\ \frac{P_3(x,y) - P_2(x,y)}{P_2(x,y) - P_1(x,y)} \ . \qquad (80)$$

Heterodyne interferometry

In heterodyne interferometry the reference wave R is frequency shifted with respect to the object wave O, e.g. with the help of acoustooptic modulators [7]. This corresponds to a linearly decreasing phase with time:

$$\psi_r(x,y,t) = \psi_{r0}(x,y) - \Delta\omega t \ . \qquad (81)$$

The two interfering light waves give then rise to a harmonically modulated intensity

$$I(x,y,t) = |O|^2+|R|^2+2|OR|\cos[\Delta\omega t+\psi(x,y)-\psi_r(x,y)]. \qquad (82)$$

The phase $\psi-\psi_r$ of this modulation can be measured electronically. Thus ψ can be obtained imediately, exept for a constant bias term.

The heterodyne technique has the disadvantage that integrating detectors, like TV cameras or CCD arrays, can not be applied. On the other hand it is more accurate than the digital interferometry method. The typical resolution is

$\lambda/1000$ [25]. That is the reason why this technique has been applied for the experimental phase determination in the present work.

3.4.2 Phase sampling in the Fourier spectrum

The sampling scheme

In Section 3.3 it was shown, that the phase sampling for moment retrieval must yield the derivatives of the phase ψ at the origin of the Fourier plane, or equivalently, the Taylor expansion terms of ψ. The minimum number of samples needed to recover the N expansion terms of order n and lower is evidently

$$N = (n+1)(n+2)/2 \; . \tag{83}$$

This number is sufficient, if the mutual position of the sampling points fulfills certain conditions. This can be seen by looking at how the expansion terms are obtained from the samples. Consider the Taylor expansion of the phase $\psi(p,q)$ up to order n:

$$\psi_n(p,q) = a_1 + a_2 p + a_3 q + a_4 p^2 + \ldots + a_N q^n \; . \tag{84}$$

In the sampling domain the two functions ψ and ψ_n should be similar (Sec.3.3). So one gets the following relation between the sampled values ψ^i and the expansion terms a_k.

$$\psi^i = \psi(p_i,q_i) \simeq \psi_n(p_i,q_i) =$$

$$a_1 + a_2 p_1 + a_3 q_i + a_4 p_i^2 + \ldots + a_N q_i^n \; , \; i = 1 \ldots M \; : \tag{85}$$

Approximations a_k' of the a_k can thus be deduced from the M equations

$$\psi^i = a_1' + a_2' p_i + a_3' q_i + a_4' p_i^2 + \ldots + a_N' q_i^n \; , \; i = 1 \ldots M \; , \tag{86}$$

provided that $M \geq N$, and at least N N-tuplets $(1, p_i, q_i, p_i^2, \ldots, q_i^n)$ are linearly independent. So the N expansion terms a_k' of order n and lower can be uniquely recovered from N samples taken at properly chosen coordinates p_i, q_i. If the number of samples M exceeds N, the a_k' may be overdetermined by the Eqs.(86). In

this case it is adequate to choose the a'_k the way that the polynomial $\psi_n(p,q) = a'_1 + a'_2 p + \ldots + a'_N q^n$ is a least square fit to the samples ψ^i:

$$\sum_{i=1}^{M} [\psi^i - \psi_n(p_i,q_i)]^2 = \min . \qquad (87)$$

In practical applications it is convenient to work with rectangular regular detector arrays. Symmetric arrays are preferable, since they are well matched to the hermitian Fourier spectra. These properties are offered by the diamond shaped detector array (Fig.27) put forward by Teague [20].

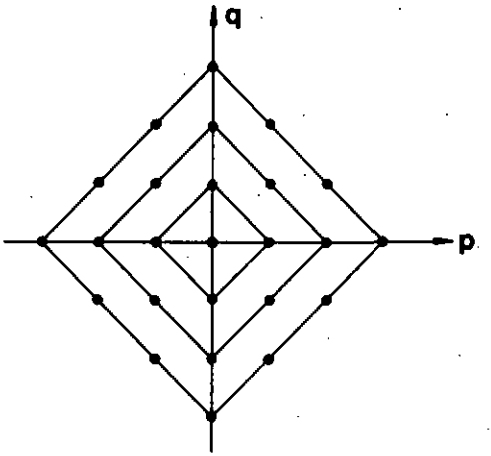

Fig.27. Diamond shaped sampling array for the detection of derivatives (or Taylor expansion terms) at the origin.

Teague proposed to determine the constant term a'_1 from the center sample, the linear (first order) terms a'_2, a'_3 from the samples on the first ring, the second order terms from the second ring plus the center sample, and so forth, including one more ring for every additional order. This method requires many detectors and does not offer optimal redundance, since it uses only a small fraction of the total number of samples for the determination of a given expansion term. The following Table shows that the least square fit concept (Eq.(87)) yields more terms for the same sampling array.

		Teague method:		least square method:	
number of rings in the array	number of samples in the array	highest detected order	number of detected terms	highest detected order	number of detected terms
0	1	0	1	0	1
1	5	1	3	1	3
2	13	2	6	3	10
3	25	3	10	5	21

Table 1. Taylor expansion terms obtained from the diamond shaped detector array of Fig.27.

The diamond shaped detector array and the least square fit concept are well suited for the present task and will be applied in the following.

The sampling interval

A well known result of the sampling theory says that bandlimited functions can be exactly recovered from the samples, provided the sample spacings are smaller than a certain value. This "sampling theorem" was discovered by Whittaker and popularized by Shannon [6]. To derive it for the 1-D case, we consider a function g(x), sampled at intervals d (Fig.28). The selected information is given by the product of g(x) and the sampling function, which consists of a set of equidistant delta functions. Thus the Fourier spectrum is equal to the convolution of the spectra of g(x) and the sampling function (Fig.28).

If the highest spatial frequency (r) contained in g(x) is smaller than 1/2d, the central part G(p) of the spectrum can be selected and Fourier transformed to yield the original function g(x) (Fig.28). This way the function is exactly recovered from samples taken at intervals d, if

$$d \leq 1/2r \,. \qquad (88)$$

Equation (88) is called the Nyquist criterion. It says that the sampling frequency must be at least twice the highest frequency component of the function to be sampled.

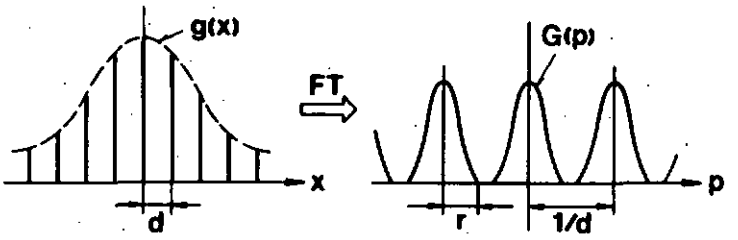

Fig.28. Sampled function g(x) and resulting Fourier spectrum. G(p) and g(x) are Fourier transform pairs.

Now, strictly speaking, a spatially bounded function g(x), such as the Fourier spectra to be sampled, is not bandwidth limited [26] and the Nyquist criterion can not be applied. But in most applications only a very small fraction of the spectral information is lost by the limited aperture of the optical system. So the spectrum can be recovered approximately from the samples taken at intervals given by Eq.(88). Note, however, that this requires the sampling array to cover all of the spatially bounded spectrum. Sampling only a fraction is equivalent to a further truncation of the spectrum. If the sampling domain is even limited to the zero diffraction order, as was found to be necessary for the extraction of some low order moments from a small number of samples, the suitable sampling interval is no longer given by Eq.(88).

An adequate sampling interval for this case can be determined from the sampling domain (discussed in Sec.3.3) and the sampling array geometry. In the example given by Fig.26 the Taylor expansion up to order three (ψ_3) is a good approximation of the phase ψ for $|pc| \leq 1$ and $|qc| \leq 1$. The adequate sampling array for the detection of ψ_3 contains 13 elements and measures four by four sample spacings (Fig.27, Tab.1). This array should extend over the domain

$|pc|, |qc| \leq 1$, which yields a sample spacing of $s = 1/2c$. Thus the sampling interval is given by the object extension c. In practice it will be appropriate to match the sample spacing to the largest object extension occurring. This way the accuracy is reduced for smaller object extensions, but one avoids capital errors caused by sampling outside the proper domain.

The sample aperture

In the above discussion the sampling array was represented by a set of delta functions. In practice the samples are taken by detectors with finite apertures. Often, the aperture size is not small compared to the detector spacing, so that the samples differ considerably from what is obtained from δ-type sampling. The effect of an extended sample aperture can be determined as follows [27].

Consider a two-dimensional function $F(p,q)$, which is sampled at the coordinates p', q' by detectors with the aperture function $P(p-p',q-q')$. The resulting samples $F_s(p',q')$ are given by

$$F_s(p',q') = \int_{-\infty}^{\infty}\int F(p,q)\, P(p-p',q-q')\, dp\, dq \,. \qquad (89)$$

The integral in Eq.(89) is a convolution of $F(p,q)$ and $P(-p,-q)$. Thus the finite size aperture acts as low pass filter. This filter has an impuls response given by the aperture function $P(p,q)$, or equivalently, a transfer function corresponding to the Fourier transform of $P(p,q)$. Sampling $F(p,q)$ with extended detectors is equivalent to δ-type sampling of the filtered version $F_s(p',q')$. The filtering effect can be compensated, if necessary, because the filter function is known [28,29]. It will be neglected in the following, since it causes errors of minor importance.

3.4.3 Determination of the irradiance moments

As was shown in Section 3.3, the normalized third order irradiance moments of an object are given by the corresponding Taylor expansion terms of the phase in the Fourier spectrum (Eq.(75)). Approximations of these terms are the monomial components of a polynomial ψ_n fitted to the phase samples (see 3.4.2). Such a polynomial least square fit can be calculated from the proper derivatives of Eq.(87). A more elegant method consists in the projection of the sampled phase

$$\psi_\delta(p_i,q_i) = \iint \psi(p,q)\ \delta(p-p_i,q-q_i)\ dp\ dq \qquad (90)$$

onto a number of orthonormal basis functions

$$B_k(p,q) = b_{k1} + b_{k2}p + b_{k3}q + \ldots + b_{kN}q^n\ , \qquad (91)$$

which yields the B_k-components in the desired least square fit polynomial ψ_n. So with the appropriate scalar product [,] one finds

$$\psi_n(p,q) = \sum_{k=1}^{N} c_k\ B_k(p,q)\ , \quad \text{where} \qquad (92)$$

$$c_k = [\psi_\delta(p,q),B_k(p,q)] \qquad \text{and} \qquad (93)$$

$$[B_i,B_k] = \delta_{ik}\ . \qquad (94)$$

The scalar product must be matched to the sampling array. If delta-type samples are taken in the coordinates p_i,q_i, the product may be defined as

$$[\psi_\delta,B_k] = \sum_{i=1}^{M} \psi_\delta(p_i,q_i)\ B_k(p_i,q_i)\ . \qquad (95)$$

A set of orthonormal functions can be constructed from the generating monomials $1,p,q,p^2,pq,q^2 \ldots q^n$ by means of the Gramm-Schmitt procedure.

Evidence for the least square fit property of polynomials obtained by the discribed method (Eqs.(92)-(94)) is found in text books on linear algebra.

The following example is based on the sampling array chosen for experimental investigations (Fig.29). The central array element will be used as reference for the phase detection, thus it is not considered as a sample. The remaining M=12 samples a...m allow to recover approximations of the 10 Taylor expansion terms of order three and lower.

The least square fit procedure starts with the construction of N=10 basis functions B_k, which are orthonormal with respect to the scalar product given in Eq.(95). The B_k in Eq.(96) result from the application of the Gramm-Schmitt method to the generating monomials $1,p,q,...q^n$. p_s and q_s are the normalized coordinates p/s and q/s, respectively.

$$
\begin{aligned}
B_1 &= 1/(12)^{1/2} \\
B_2 &= p_s/(14)^{1/2} \\
B_3 &= q_s/(14)^{1/2} \\
B_4 &= (6p_s^2-7)/(780)^{1/2} \\
B_5 &= p_s q_s/2 \\
B_6 &= (37p_s^2+65q_s^2-119)/(61880)^{1/2} \\
B_7 &= (7p_s^3-19p_s)/(1512)^{1/2} \\
B_8 &= (7p_s^2q_s-2q_s)/(140)^{1/2} \\
B_9 &= (9p_sq_s^2+2p_s^3-8p_s)/(108)^{1/2} \\
B_{10} &= (140q_s^3+336p_s^2q_s-476q_s)/(282240)^{1/2}
\end{aligned}
\qquad (96)
$$

Application of Eqs.(93) and (92) yields then the polynomial $\psi_n(p,q)$, which is fitted to the samples a...m (Fig.29):

$$\psi_n(p,q) =$$

$$(1/8)\,[2(c+f+g+k)+(b+d+i+\ell-a-m-h-e)] \qquad (97)$$

$$+\ (1/12)\,[8(g-f)-(h-e)]\ p/s$$

$$+\ (1/12)\,[8(c-k)-(a-m)]\ q/s$$

$$+\ (1/952)\,[141(h+e)+29(a+m)-17(b+d+i+\ell)-54(g+f)-82(c+k)]\ (p/s)^2$$

$$+\ (1/4)\,[d+i-b-\ell]\ (pq/s^2)$$

$$+\ (1/952)\,[141(a+m)+29(h+e)-17(b+d+i+\ell)-54(c+k)-82(g+f)]\ (q/s)^2$$

$$+\ (1/12)\,[(h-e)+2(f-g)]\ (p/s)^3$$

$$+\ (1/4)\,[(b+d-i-\ell)+2(k-c)]\ (p^2q/s^3)$$

$$+\ (1/4)\,[(d+\ell-b-i)+2(f-g)]\ (pq^2/s^3)$$

$$+\ (1/12)\,[(a-m)+2(k-c)]\ (q/s)^3.$$

A comparison with the Eq.(75) shows, that the odd terms in Eq.(97) yield the third order moments of the object function. The even terms vanish, since the real valued object has a hermitian Fourier spectrum. However, in practice the sampled phase will not be perfectly an odd function. The resulting even terms of the fitted polynomial are therefore convenient error indicators. A constant term represents a bias in the phase detection, which may result from unbalanced input channels or from an offset of the phasemeter. Quadratic terms may occur due to wave front distortions in the object plane or due to an axial shift between sampling plane and Fourier plane. Finally the mean square difference between the sampled phase and the fitted polynomial

$$D = (1/12) \sum_{i=1}^{12} [\psi_\delta(p_i,q_i) - \psi_n(p_i,q_i)]^2 \qquad (98)$$

indicates the accuracy of the determination of Taylor expansion terms and moments. This indicator is reliable, if the number of samples M exceeds considerably the number of recovered monomial terms N.

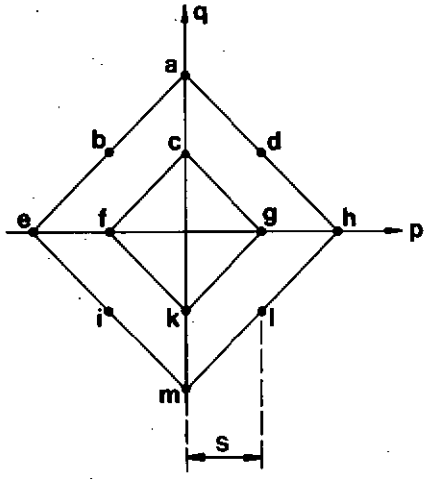

Fig.29. Sampling array in the Fourier plane used for computer simulated and experimental moment detection.

Computer simulations

The accuracy of the moment detection depends strongly on the object function and the sampling scheme. Error estimations for the general case yield therefore only very poor results. More information was obtained from a computer simulation for a particular case. For this purpose the binary triangular object given in Fig.30 was chosen. (Note that the object must not have central symmetry, otherwise the odd central moments vanish). The phase ψ in the Fourier spectrum of this triangle was then calculated for the 12 sampling points represented in Fig.29. Finally a polynomial of third order was fitted to the sampled phase using Eq.(97).

Table 2 shows the result for a normalized sample spacing of sc = 0.3. The blocks of numbers are arranged according to the corresponding position in the applied sampling array (Fig.29). The three numbers in each block represent from

top to bottom: sampled phase, function value of the fitted polynomial, difference of the two (in degrees). The center number (0.000) is the constant term of the polynomial fitted to the 12 samples taken outside the center.

The vanishing differencies in Tab.2 show that the polynomial fits perfectly to the 12 samples. This is due to the fact that the object function is real valued, and therefore the phase is an odd function with respect to the origin, which causes exact odd symmetry for the calculated phase samples. As a result of this symmetry, the number of independent samples is reduced to 6, and the corrresponding polynomial with its 6 terms of order 1 and 3 can be perfectly fitted. The even terms of the least square fit polynomial are obviously equal to zero.

		1.838		
		1.838		
		0.000		
	0.122	0.212	-0.160	
	0.122	0.212	-0.160	
	0.000	0.000	0.000	
-1.125	-0.133		0.133	1.125
-1.125	-0.133	0.000	0.133	1.125
0.000	0.000		0.000	0.000
	0.160	-0.212	-0.122	
	0.160	-0.212	-0.122	
	0.000	0.000	0.000	
		-1.838		
		-1.838		
		0.000		

Table 2. Array of blocks containing each from top to bottom: calculated phase samples, value of the fitted third order polynomial, difference of the two (all in degrees). The sampling array and the object are given by the Figs.29 and 30. The normalized sample spacing is sc = 0.3.

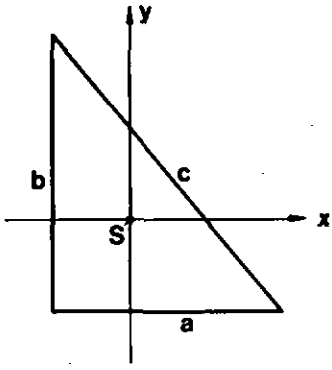

Fig.30. Binary triangular object chosen for computer simulation of the moment detection (b/a = 1.17). The object centroid is at the origin of the x,y plane.

The central moments of order three can be deduced up to the constant factor m_{00} from the third order terms of the fitted polynomial (see 3.3). The corresponding normalized moments $\mu_{jk} = m_{jk}/m_{00}^{(j+k+2)/2}$ are given in Tab.3, together with their exact values. As can be expected, the accuracy of the recovered moments decreases with growing sample spacings sc. The latter must be smaller than sc = 0.3, if the third order moments are to be detected to better than 15%.

Very small sample spacings yield accurate results in computer simulations, but not in practical applications. This is due to the limited accuracy of the experimental phase detection. The phase values to be sampled decrease rapidly for smaller sample spacings, so that the relative error in the phase detection becomes important. The largest detected phase value ψ_{max} within the array is some 1.8 deg for sc = 0.3 (Tab.3). A typical accuracy of 0.2 deg for heterodyne phase detection yields thus an error of 10 to 20% (depending on the error of each sample).

This implies that it is not trivial to detect these moments accurately with this approach. A considerable improvement of the accuracy requires more samples to detect more Taylor expansion terms. But this yields no further moments if only the phase of the Fourier spectrum is detected (see 3.3).

	exact value	obtained from phase sampling				
		sc=0.1	0.2	0.3	0.4	0.5
μ_{30}	.0166	.0168	.0174	.0182	.0196	.0217
μ_{21}	-.0097	-.0095	-.0098	-.0098	-.0099	-.0100
μ_{12}	-.0113	-.0111	-.0115	-.0116	-.0119	-.0123
μ_{03}	.0264	.0267	.0281	.0300	.0331	.0383
ψ_{max}		.0621	.5179	1.838	4.724	10.43

Table 3. Normalized moments $\mu_{jk} = m_{jk}/m_{00}^{(j+k+2)/2}$ *obtained from exact calculations and from phase sampling in the Fourier plane (computer simulation). Object and sampling array are shown in the Figs.30 and 29, sc is the normalized sample spacing.* ψ_{max} *denotes the largest detected phase value within the array (in deg).*

3.4.4 Experimental investigation

3.4.4.1 The set-up

The phase sampling in the zero order spot of Fourier spectra was experimentally tested with a set-up according to Fig.31. The heterodyne interferometer contains a Fourier processor (3...9) in one branch and in the other branch a pair of acoustooptic modulators (14) which shift the frequency of the reference beam by 100 kHz. This beam is expanded, truncated by a

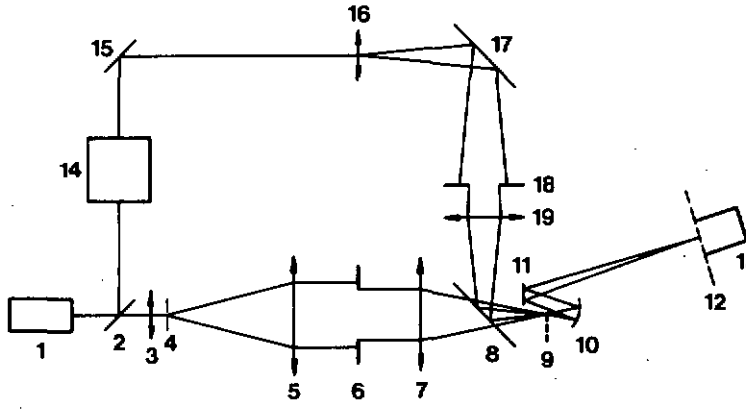

1	He-Ne laser 5 mW (Aerotech Inc. LSR5PD)
2,8	beam splitter cube (CVI)
3	microscope objective 40x (S+H)
4	pin-hole 15 µm
5,7	Fourier lens f = 380 mm (SORL FX15/5F).
6	object-mask
9	Fourier plane
10	concave sherical mirror f = 12.5 mm (S+H)
11,15,17	mirror
12	detection plane
13	detection unit
14	acoustooptic modulators (Intra Action AOM-40)
16	achromate lens f = 30 mm (S+H)
18	circular aperture d = 6 mm
19	precision achromate lens f = 240 mm (Melles Griot)

Fig.31. Set-up of the heterodyne interferometer used for the phase sampling in the zero order spot of the Fourier spectrum. The detector unit (13) and the electronics for the phase measurement are given in detail in Figs.32 and 33.

circular aperture (18) and focused onto the center of the Fourier plane (9), so that an Airy diffraction pattern is superposed to the Fourier spectrum. The central Airy disk represents a convenient reference wave for the phase sampling, since it has a plane wave front and a high light intensity. To obtain a good wave front flatness in practice, this disk was chosen to have at least twice the size of the zero order spots to be sampled. The unequal lengths of the two interferometer branches are due to practical considerations. The difference of the path lengths was twice the cavity length of the laser (1), which yields again maximum contrast for the interference fringes. The wave front distortions in the Fourier processor were kept small by using only the cental domain of both Fourier lenses (5,7) and the beam splitter (8).

In the present set-up the Fourier spectrum had to be magnified by about a factor of 50 to match the size of the detector array. This magnification can be achieved by means of an appropriate standard microscope objective. The resulting image of the spectrum, however, tends to be visibly degraded due to dust particles on the objective and stray reflections. The first effect can be reduced by application of an objective with a long focal length, so that dust particles become small compared to the cross section of the light beam. The second is diminished by using a single properly coated lens. Still considerably better results were obtained with a concave spherical mirror (10). The astigmatism introduced by the somewhat oblique incidence of the light beam was small enough to be negligible.

An accurate measurement of the optical phase requires fast detectors, which transform the local intensity modulation (100 kHz heterodyne frequency) into electrical signals of essentially the same phase. The tolerable phase shift introduced by the detector is approximately 0.5 deg for the present application. (This retardation is partly compensated by the same effect in the reference channel, so that the resulting contribution to the error in the phase measurement does not exceed 0.1 deg.) This is assured by using detectors with a bandwidth of some 100 times the heterodyne frequency, i.e. 10 MHz. The sampling is done serially by two photomultipliers and an optical multiplexer, rather than using 13 fast detector-amplifier units to realize the sampling scheme given in Fig.29.

Fig.32 shows the set-up of the applied detector unit. The magnified Fourier spectrum in the detection plane is sampled by a diamond shaped array of 13 optical multimode fibers (1). The central fiber leads to the photomultiplier (10), which provides the reference signal for the electronic phasemeter. The 12 remaining fiber outputs are linearly arranged in some plane (4). These are imaged on the filter plane (8), where a vertical slit masks all but one of them. The sample seen by the photomultiplier (9) can be selected by means of the galvanometer driven mirror (7).

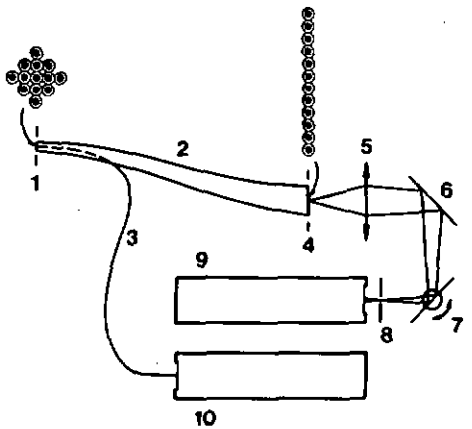

1	diamond shaped array of 13 fiber ends in the detection plane (multimode silica fibers with 200 µm core diameter spaced by 300 µm)
2	bundle of 12 fibers carrying the samples
3	central fiber carrying the reference signal
4	linear (horizontal) arrangement of the 12 fiber ends
5	imaging lens (achromat f = 40 mm)
6	mirror
7	galvanometer driven mirror (General Scanning G-300PD)
8	vertical slit masking all but one sample
9,10	photomultiplier (RCA 8645)

Fig.32. Set-up of the detector unit for phase sampling according to the sampling scheme given in Fig.29.

The harmonically modulated electric signals (100 kHz) leaving the two photodetectors are amplified and bandpass filtered before their relative phase shift is measured by a commercially available phasemeter (Fig.33). It is

evident that for an accurate phase sampling the phase shifts introduced by the amplifier-filter combinations in the two channels in Fig.33 must be small or carefully balanced. Fast operation amplifiers (gbp = 40 MHz) were therefore used to build amplifier units (3,6,9,13,16,19) with some 10 MHz bandwidth at a gain of 4.7. The phase shift caused by such an amplifier unit is less than 0.5 deg at 100 kHz, which is sufficiently small.

In the case of the filters the phase shifts are of the order of 90 or 180 deg, so that careful balancing is indispensable for an accurate phase detection. This symmetry has been achieved with adjustable low-Q bandpass filters consisting of RC elements. Metalfilm resistors and PVC capacitors were chosen to increase the temporal stability. The gain of the whole amplifier-filter unit is about 40 at 100 kHz. This gain assures a minimum signal level of 0.2 V at the input of the phasemeter, which is necessary to obtain the specified accuracy of 0.2 deg.

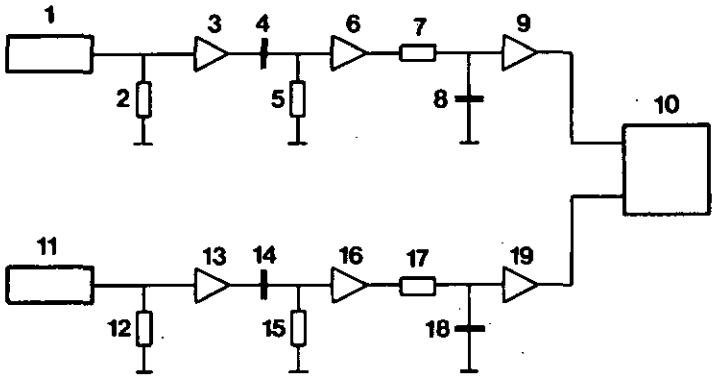

1,11	photomultiplier (RCA 8645)
2,12	resistor 1 kOhm
3,6,9,13,16,19	amplifier 10 MHz, gain 4.7
4,14	capacitor 820 pF (PVC)
5,7,15,17	resistor 1 kOhm (metalfilm) shunted by 100 kOhm pot.
8,18	capacitor 3170 pF (PVC)
10	phasemeter, 0.1 deg resolution (EVANS ASSOCIATES M 4119)

Fig.33. Electronics used for the phase measurement. The components 3..9 and 13..19 form two amplifier-filter units with a gain of 40 at 100 kHz and a logarithmically symmetric bandpass characteristic with a slope of 20 dB per decade.

The discribed evaluation of the sampled phase allows to selectively determine the different phase terms. So, for the detection of third order moments, one need not bother about a bias in the detected phase. The most harmful errors introduced by the electronics in Fig.33 are the temporal variation and the phase shift caused by unbalanced signal levels. Test measurements showed that the first was about 0.1 deg, while the second was 0.1 deg per factor two of signal level asymmetry.

3.4.4.2 Experimental phase sampling and moment retrieval

Positioning the sampling detectors

Although the Fourier plane is known to be in the back focal plane of a lens, it is not trivial in practice to determine the position of this plane accurately. Searching for the plane wave front in the zero order spot of an Airy diffraction pattern is difficult, since usual interferometric methods yield the deviations from the reference wave front rather than the absolute wave front curvature. Moreover, the development of the wave front curvature along the optical axis is complicated and not monotonious in the neighbourhood of the focal point [30].

An accurate method to detect the Fourier plane was found some 30 years ago by workers dealing with x-ray diffraction. It resulted from calculations of the intensity distribution near the focal point of a spherical converging wave. This distribution was found to be essentially symmetric with respect to the focal plane [31]. The intensity on the optical axis vanishes at multiples of a certain distance from the focal point. The position of the Fourier plane is therefore given by the points of zero intensity, which can be detected quite accurately.

The intensity distribution accross the light beam depends sensitively on a small axial shift from the focal plane, if the aperture of the focused light beam is large. The accuracy of the detection of the Fourier plane could therefore be improved by choosing larger objects than were used for the phase sampling. The typical object extension could be trebled without using more than the central domain of the Fourier lens (35 mm diam.), which causes a wave front

distortion of less than $\lambda/10$. This way the position of the Fourier plane was localized within $\Delta z = 30$ µm, so that the requirement for the present application ($\Delta z \leq 0.9$ mm, see [32]) was largely satisfied.

Centering the detector array (fiber bundle) on the optical axis was straight forward: The array was shifted in the Fourier plane until the central fiber captured maximum light power from the zero order spot of the Airy diffraction pattern belonging to a large (30 mm diam.) circular object. The estimated error (40 µm) is equal to 13% of the detector (fiber) spacing.

The desired radial position of the sampling detectors in the Fourier spectrum was obtained by choosing the proper magnification between the Fourier plane and the detection plane (Fig.31). The spectrum of a grating like object was taken as reference for the calibration.

Phase sampling

In a first attempt the samples were taken in the zero order disk of an Airy diffraction pattern. This disk has a plane wave front, so that all the sampled phase values should vanish, if the circular object is centered on the optical axis. The 12 sampled values, however, were arbitrarily spread over a range of typically -0.6...1.5 deg. This error can clearly not be neglected for the moment detection. To localize the source of error, the wave front flatness in the sampling domain was improved by extending the Airy disk diameters of both reference and object waves. Since the phase samples remained essentially the same, it was concluded that the bulk of the error is introduced by the detector unit (Fig.32).

Further evidence for this conclusion was obtained by sampling the plane wave front in spectra of objects, which are not circular, but still have a central symmetry. The sampled phase was essentially independent of the object. Consequently this phase represents a constant bias, which is superposed to the phase to be detected. The correct samples are therefore obtained by substracting this bias individually from the sampled phase values. Due to this differential measurement the moment detection becomes independent of any wave front curvatures in the reference beam. Long term variations of the sampled phase were compensated by periodically detecting the bias values to be substracted.

With this procedure the accuracy of the pase sampling was considerably improved. A typical result is represented in Tab.4. It gives the 12 phase values sampled in the spectrum of the triangular object shown in Fig.30 (top numbers), the theoretical values and the difference (bottom numbers), all in degrees. The diamond shaped array of numbers corresponds to the sampling scheme (Fig.29), the blocks of numbers are placed according to the position of the related sampling point. The normalized sample spacing was sc = 0.3.

		-0.2		
		0.000		
		-0.200		
	-0.3	-0.6	-1.6	
	-0.234	-0.707	-1.643	
	-0.066	0.107	0.043	
0.1	0.3		-0.3	-0.1
0.000	0.430	0.000	-0.430	0.000
0.100	-0.130		0.130	-0.100
	1.4	0.5	-0.1	
	1.643	0.707	0.234	
	-0.243	-0.207	-0.334	
		-0.1		
		0.000		
		-0.100		

Table 4. Phase values sampled in the spectrum of the triangular object given in Fig.30. The blocks of three numbers, which are located according to the related sampling points, give from top to bottom: measured phase, calculated phase and their difference (in deg). The normalized sample spacing is sc = 0.3.

The differences between theoretical and experimental results are less than 0.34 deg for all of the 12 samples. This is a remarkable accuracy, even for

heterodyne systems with less stringent requirements on the precision of the sampling geometry. The error of the phase detection was found to increase for larger detector spacings. The maximum relative accuracy of the samples was found for sc ≈ 0.3.

The 12 phase samples given in Tab.4 can now be evaluated according to the procedure discribed in Sec.3.4.3 to yield the phase terms up to order three in the Fourier plane and the corresponding object moments of first and third order. In a first step one determines the polynomial least square fit to the sampled phase values. Tab.5 gives the measured phase samples, the function value of the fitted third order polynomial and the difference (from top to bottom) for the 12 sampling points.

		-0.2		
		-0.225		
		0.025		
	-0.3	-0.6	-1.6	
	-0.230	-0.641	-1.530	
	-0.070	0.041	-0.070	
0.1	0.3		-0.3	-0.1
0.078	0.248	-0.063	-0.352	-0.122
0.022	0.052		0.052	0.022
	1.4	0.5	-0.1	
	1.470	0.459	-0.030	
	-0.070	0.041	-0.070	
		-0.1		
		-0.125		
		-0.025		

Table 5. Least square fit of a third order polynomial to the measured phase samples from Tab.4. The 12 blocks of numbers are located according to the related sampling point and indicate from top to bottom: measured phase sample, function value of the fitted third order polynomial and their difference (in deg).

Table 5 shows that the polynomial fits quite well to the measured samples. The root mean square difference between the samples and the corresponding function values of the polynomial is 0.05 deg. The center number in Tab.5 indicates the constant term of the polynomial and thus the bias in the phase determination (-0.063 deg). The quadratic term of the fitted polynomial is less than 0.12 deg for all of the 12 sampling points. While the even phase terms above are due to measurement errors, the odd terms are not. The linear phase components are proportional to the coordinates x_s, y_s of the object centroid. The small phase values in Tab.5 ($\psi << 180$ deg) indicate that x_s and y_s were small compared to the object extension c ($x_s/c = 0.0035$, $y_s/c = 0.0067$).

The most interesting result for the present work are the magnitudes of the four third order phase terms, or equivalently, the four detected third order central moments of the object. Table 6 gives these moments together with moments retrieved from calculated phase samples and the exact values.

	exact value	obtained from calculated phase samples (Tab.4)	obtained from calculated phase samples rounded to 0.1 deg	obtained from measured phase samples (Tab.5)
μ_{30}	.0166	.0162	.0170	.0106
μ_{21}	-.0097	-.0098	-.0085	-.0106
μ_{12}	-.0113	-.0116	-.0127	-.0170
μ_{03}	.0264	.0300	.0297	.0223

Table 6. Normalized central moments of third order $\mu_{jk} = m_{jk}/m_{00}^{5/2}$ obtained for the object and the sampling array given in Figs. 29 and 30. The normalized sample spacing is sc = 0.3.

Table 6 shows the influence of different sources of error on the accuracy of the resulting object moments. The moments retrieved from the calculated phase samples differ by up to 14% from the exact values (columns 1,2) due to

neglegting the phase terms of fifth and higher order. The rounding of the calculated phase samples to 0.1 deg causes another error of up to 13% (columns 2,3). These two error components compensate to some amount, so that the moments retrieved from the rounded phase samples differ by less than 13% from the exact values (columns 1,3). The measured phase samples in Tab.5, which differ by up to 0.33 deg from the exact values, yield moments with up to 50% deviation from the correct values (columns 1,4).

These typical results show clearly, that highly accurate phase sampling is indispensable, if the moments are to be determined to better than 10%. Moreover, this condition requires the phase terms of fifth order to be considered (Tab.6, columns 1,2), so that the diamond shaped detector array must be extended to 25 sampling elements (Tab.1). The requirement on the sampling accuracy is still higher for objects with a less pronounced asymmetry, which generate smaller third order phase terms in the Fourier spectrum. It must be concluded from these results, that it is difficult in practice to detect moments of third and higher order accurately by sampling the phase in the Fourier plane. The feasibility of an object recognition concept based on the comparison of the resulting moments is therefore rather disproved.

Although the accuracy of the measured moments is rather poor, it might be sufficient to resolve the 180 deg ambiguity in the determination of the object orientation described in Section 2.1. The reliability of this method was tested by shifting an object accross the field of vision and sampling the resulting phase distribution in the zero order spot of the Fourier spectrum. The central moments of third order were then retrieved from these samples. The typical values in Tab.8 demonstrate the trend of the results.

As can be seen from Tab.7, the accuracy of the moment detection decreases, when the object centroid is shifted off the optical axis. This is not very surprising, since the object shift causes a superposed linear phase term, which dominates by far the third order terms to be determined. The moment detection suffers therefore from additional errors caused by the reduced absolute accuracy of the phasemeter and by the neglected finite extension of the sampling apertures.

object shift

y_s/c	.007	.103	.199	.295	exact
$\Delta\psi$[deg]	0	40	80	120	value
μ_{30}	.0106	.0106	.0074	.0032	.0166
μ_{21}	-.0106	-.0064	-.0096	.0042	-.0097
μ_{12}	-.0170	-.0170	-.0202	-.0234	-.0113
μ_{03}	.0223	.0287	.0234	.0350	.0264

Table 7. Normalized central moments $\mu_{jk} = m_{jk}/m_{00}^{5/2}$ of order three obtained from phase sampling in the spectrum of the triangle given in Fig.30. y_s/c is the normalized object shift and $\Delta\psi$ the resulting phase difference between the outermost detectors (a,m, Fig.29). Exact values for the object moments are added for comparison.

The 180 deg ambiguity in the determination of the object orientation can be resolved by looking at the third order phase terms in the Fourier spectrum or equivalently by evaluating the object moments of third order (see 2.2.3). Since a 180 deg rotation of the object inverts the signs of these moments, one can, in principle, resolve the ambiguity easily by comparing the signs of the detected moments and the reference moments. However, the low accuracy of the detected moments (Tab.7) indicates that some more elaborate criterion must be used to obtain a reliable decision.

A convenient method to resolve the 180 deg ambiguity is discribed in Sec.2.2.3: The angular distribution of the measured third order phase term is compared to the two reference distributions, which belong to the two opposite object orientations to be distinguished. The better coincidence indicates the correct object orientation. Note, that the phase terms are given by the object moments. Comparing third order phase terms is therefore equivalent to comparing third order moments. The phase terms can be compared in an integral manner by calculating the correlation of the angular phase distribution (Eq.(22)). Writing the correlation in terms of object moments (Eq.(24)) yields a reliable rule for the comparison of the object moments.

An example may show the efficiency of the method. For this purpose the moments from Tab.7 have been utilized. The exact moments are taken as reference values while both detected and exact moments are taken as test moments. Using Eqs.(24) and (25), the normalized values $C(\alpha_0)/C_r$ of the correlation function are calculated and the results are shown in Tab.8. The sign of $C(\alpha_0)/C_r$ is a reliable indicator of the object orientation (α_0 or α_0+180 deg), if $|C(\alpha_0)/C_r|$ is not too far from unity.

Table 8 shows that $|C(\alpha_0)/C_r|$ is nearly equal to the nominal value 1, independent of the object shift. This prooves that the 180 deg ambiguity in the determination of the object orientation can be resolved reliably by the discribed method.

	object shift				
y_s/c	.007	.103	.199	.295	for exact moments
$\Delta\psi$[deg]	0	40	80	120	
$C(\alpha_0)/C_r$	0.901	1.050	0.928	1.177	1.000

Table 8. Resolution of the 180 deg ambiguity in the detection of the object orientation: The values $C(\alpha_0)/C_r$ of the normalized correlation are calculated from Eqs.(24) and (25) with the moments given in Tab.7.

3.4.4.3 Error discussion

The most important sources of error in the detection of irradiance moments by phase sampling in the Fourier plane are discussed in the following. The error caused by neglegting the phase terms of fifth and higher order has been discribed in Section 3.4.3. It is of systematic kind and not due to experimental limitations.

The repeatability of the phase detection was mainly limited by air turbulences in the optical paths of the heterodyne interferometer. Although the set up was shielded by plastic boards, mixing of warm and cold air caused the detected phase to fluctuate by 0.1 to 0.2 deg. Similar results were obtained by Massie [33], who enclosed the light beams in tubes to get rid of the problem.

Dust particles on the optical components represent another typical source of error in coherent optical systems. The effect becomes important, where the diameter of the light beam is not very large compared to the extension of the dust particles. This was avoided in the present case by an adequate lay-out of the interferometer. Evidence for the efficiency of this precaution results from the fact that no visible structures move accross the Fourier spectrum when the optical components are slightly shifted. Dust on the fiber ends in the optical multiplexer affects the coupling efficiency, but not the phase of the intensity oscillation to be transmitted.

Stray reflections on the surface of optical elements cause extraneous fringes, which contribute to the error in the phase sampling. A careful coating of the surfaces does often not yield sufficient attenuation of the reflected light. A V-coated surface, for example, reflects typically 0.3% of the light intensity. If this stray light interferes with the main beam, it causes a phase shift of up to 3.1 deg. The error may still be more serious, if the stray reflection is focused on the detection plane. The bulk of the stray reflection in the detection plane (12) in Fig.31 was eliminated by using a concave mirror (10) instead of a microscope objective for the magnification of the Fourier spectrum.

The error in the phase detection introduced by dust particles and stray reflections are extensively discussed by Schwider et al. [24]. A rough estimation for the present case can be obtained as follows: Since the fringes caused by dust and stray light were too week to be seen in an Airy diffraction pattern, the intensity modulation in an outer (say third order) ring must have been smaller than some 10%. This modulation corresponds to a relative stray light amplitude of 2.5% in the third order ring or of 0.1% in the center of the Airy pattern. The resulting phase shift in the center of the Airy disk is less than 0.06 deg.

The geometry of the sampling array was quite accurate, since all the spacings were given by the diameter of the silica fiber (300 µm ± 3 µm). The position of the array with respect to the optical axis, however, could not be adjusted to better than 40 µm. This leads to an error in the detected phase of up to some 0.1 deg for the triangular object (Fig.30) and a sample spacing of

sc = 0.3. Neglecting the finite extension of the sampling apertures (200 µm) causes another error of up to 0.15 deg for sc = 0.3.

The optical multiplexer (Fig.32) introduces an additional error to the phase sampling. This can be concluded from the fact that the 12 phase values sampled in an Airy disk were not exactly zero (-0.5...1.5 deg) but essentially independent of the extension of the two Airy disks generated by object- and reference wave in the sampling plane. Consequently the optical path lengths through the multiplexer were not equal for the two interfering waves. It has already been mentioned that this error can, in principle, be compensated by substraction of the corresponding phase samples. However, the detected error terms were not exactly reproducable. The samples taken in Fourier spectra with a theoretically plane wave front varied by up to 0.2 deg when the multiplexer unit was moved back and forth. An error of some 0.2 deg subsists therefore after the mentioned compensation.

The electronic components, namely amplifier, filter and phasemeter, introduce essentially three types of errors. The first one consists in a bias of the detected phase, which is eliminated by the substraction of the samples taken in Airy disks. The second one is more serious, since it causes a phase shift related to the asymmetry of the signal levels in the two channels. These levels vary by about a factor of 2 and the resulting phase shift is less than 0.1 deg. A third source of error results from the limited linearity of the phasemeter response. This affects mainly the accuracy of the large phase values sampled in the spectra of objects shifted off the optical axis. The resulting error is smaller than 0.2 deg according to the specifications given by the manufacturer of the phasemeter.

The above discussion shows that the phase sampling suffers from many sources of error of similar importance. A significant improvement of the accuracy requires therefore several modifications in the measuring system. The most important measures to propose are: reduction of the air fluctuation in the light beams, reduction of the sampling apertures, improvement of the accuracy of multiplexer and phasemeter.

3.5 Conclusion

The moments of object functions have very convenient features for the characterization and recognition of objects: Moments of lowest order give a rough estimate of the object shape and more details are added when higher order moments are included. The transformation properties of moments are simple when the object function is modified by shift, scale change, rotation and inversion. Adequate linear combinations of moments are invariant to the above object transformations. Moments are remarkably independent on small object deformations.

These moments are given, according to the moment theorem, by the derivatives of the Fourier spectrum at the origin. Since Fourier transformations are easily obtained in coherent optics, it seems very attractive to detect irradiance moments of objects by extracting the derivatives from the sampled spectrum. Corresponding propositions were made [19,20], but to our knowledge, no thorough theoretical investigations or experimental feasibility tests have been carried out so far.

The results and the error discussion given above show clearly, that it is difficult to detect moments up to third order accurately from the sampled phase in the Fourier spectrum. The moment retrieval from the sampled intensity or from combined intensity and phase sampling suffers from essentially the same limitations: The intensity sampling yields only central moments of order 0, 2 and 4 (Eq.71). The detection of the sixth order moments requires knowledge of the third order moments (or phase terms) in addition to the intensity terms up to sixth order. As these third order terms can not be detected reliably, the best one can retrieve even from combined phase and intensity sampling are the moments of order 0, 1, 2 and 4. Moreover, intensity and phase sampling have many error sources in common, which shows, together with the estimation of the accuracy given in Sec.3.3, that it is difficult to detect moments of fourth order accurately.

References

1. A. Vander Lugt, "Signal detection by complex spatial filtering", IEEE Trans. Inf. Theory IT-10, 139-146 (1964).

2. A.D. Gara, "Real-time tracking of moving objects by optical correlation", Appl. Opt. 18, 172-174 (1979).

3. A.D. Gara, "Optical computing for image processing", in "Computer vision and sensor-based robots", G.G. Dodd and L. Rossol, Eds. (Plenum, New York, 1979), pp. 207-234.

4. R. Dändliker, K. Hess, Th. Sidler, "Hybrid coherent optical and electronic object recognition", Appl. Opt. 22, 2081-2086 (1983).

5. C.B. Johnson, S. Nevin, J. Sebris and J.S. Abshire, "Circular-scan streak tube with solid-state readout", Appl. Opt. 19, 3491-3495 (1980).

6. C.E. Shannon, "Communication in the presence of noise", Proc. IRE 37, 10-21 (1949).

7. R. Dändliker, "Heterodyne holographic interferometry", in "Progress in optics" (North Holland, Amsterdam, 1980), Vol. 17, pp. 40-84.

8. J.D. Gaskill, "Linear systems, Fourier transforms, and optics" (Wiley, New-York, 1978), pp. 179-217.

9. J. Radon, "Ueber die Bestimmung von Funktionen durch ihre Integralwerte längs gewisser Mannigfaltigkeiten", Ber. Saechs. Akad. Wiss. 69, 262-278 (1917).

10. G.J. Agin, "Computer vision systems for industrial inspection and assembly", Computer 13, 11-20 (1980).

11. S.A. Dudani et al., "Aircraft identification by moment invariants", IEEE Trans. Comput. C-26, 39-45 (1977).

12. N.B. Nill, "Contrast effect on imagery power spectra", Appl. Opt. 18, 2147-2151 (1979).

13. M.G. Kendall and A. Stuart, "The advanced theory of statistics" (Charles Griffin Comp.Ltd., London, 1969), Vol.1, pp. 118-120.

14. M.R. Teague, "Image analysis via the general theory of moments", J. Opt. Soc. Am. 70, 920-930 (1980).

15. M. Born and E. Wolf, "Principles of optics" (Pergamon Press, Oxford, 1980), pp. 464-465.

16. M.K. Hu, "Visual pattern recognition by moment invariants", IRE Trans. Inf. Theory IT-8, 179-187 (1962).

17. D. Casasent et al. "Optical systems to compute intensity moments: design", Appl. Opt. 21, 3292-3298 (1982).

18. J.A. Blodgett et al., "Multiplexed coherent optical processor for calculating generalized moments", Opt.Lett. 7, 7-9 (1982).

19. A.F. Fercher, "Pattern recognition by optical moments", Opt. Comm. 20, 81-85 (1977).

20. M.R. Teague, "Optical calculation of irradiance moments", Appl. Opt. 19, 1353-1356 (1980).

21. A. Papoulis, "Systems and transforms with applications in optics" (McGraw-Hill, New-York, 1968), pp. 77-78.

22. J.C. Wyant, "Interferometric optical metrology: basic principles and new systems", Laser Focus 18, No.5, 65-71 (1982).

23. J.H. Bruning et al., "Digital wavefront measuring interferometer for testing optical surfaces and lenses", Appl. Opt. 13, 2693-2703 (1974).

24. J. Schwider et al., "Digital wave front measuring interferometry: some systematic error sources", Appl. Opt. 22, 3421-3432 (1983).

25. J. Mastner and V. Masek, "Electronic instrumentation for heterodyne holographic interferometry", Rev. Sci. Instrum. 51, 926-931 (1980).

26. F.T.S. Yu, "Optics and information theory" (J. Wiley, New York, 1976), pp. 150-154.

27. J.R. Leger and S.H. Lee, "Signal processing using hybrid systems", in "Applications of optical Fourier transforms", H. Stark (Academic Press, New York 1982), pp. 146-147.

28. J.L. Harris, "Image evaluation and restoration", J.Opt.Soc.Am. 56, 569-574 (1966).

29. C.W.Helstrom, "Image resrtoration by the method of least squares", J.Opt.Soc.Am. 57, 209-303 (1967).

30. M. Born and E. Wolf, "Principles of optics" (Pergamon Press, Oxford, 1980), pp. 444-447.

31. B.J. Thompson, "Optical transforms and coherent processing systems", in "Optical data processing", D. Casasent (Springer, Berlin, 1978), pp.31-33.

32. S.H. Lee, "Basic principles of optical information processing" in "Optical information processing", S.H. Lee (Springer, Berlin, 1981), pp. 36-37.

33. N.A. Massie et al., "Measuring laser flow fields with a 64-channel heterodyne interferometer", Appl. Opt. 22, 2141-2151 (1983).